SANDIA REPORT

SAND2003-4381
Unlimited Release
Printed January 2004

Computational and Experimental Techniques for Coupled Acoustic/Structure Interactions

Timothy F. Walsh, Garth M. Reese, Kendall H. Pierson, Hartono Sumali, Jeffrey L. Dohner, and David M. Day

Prepared by
Sandia National Laboratories
Albuquerque, New Mexico 87185 and Livermore, California 94550

Sandia is a multiprogram laboratory operated by Sandia Corporation,
a Lockheed Martin Company, for the United States Department of Energy under Contract DE-AC04-94AL85000.

Issued by Sandia National Laboratories, operated for the United States Department of Energy by Sandia Corporation.

Available to DOE and DOE contractors from
U.S. Department of Energy
Office of Scientific and Technical Information
P.O. Box 62
Oak Ridge, TN 37831

Telephone: (865)576-8401
Facsimile: (865)576-5728
E-Mail: reports@adonis.osti.gov
Online ordering: http://www.doe.gov/bridge

Available to the public from
U.S. Department of Commerce
National Technical Information Service
5285 Port Royal Rd
Springfield, VA 22161

Telephone: (800)553-6847
Facsimile: (703)605-6900
E-Mail: orders@ntis.fedworld.gov
Online order: http://www.ntis.gov/ordering.htm

SAND2003-4381
Unlimited Release
Printed January 2004

Computational and Experimental Techniques for Coupled Acoustic/Structure Interactions

Timothy F. Walsh, Garth M. Reese, and Kendall H. Pierson
Computational Solid Mechanics and Structural Dynamics

Hartono Sumali
Structural Dynamics Research

Jeffrey L. Dohner
MEMS Device Technologies

David M. Day
Computational Mathematics

Sandia National Laboratories
P.O. Box 5800
Albuquerque, New Mexico 87185

Abstract

This report documents the results obtained during a one-year Laboratory Directed Research and Development (LDRD) initiative aimed at investigating coupled structural acoustic interactions by means of algorithm development and experiment. Finite element acoustic formulations have been developed based on fluid velocity potential and fluid displacement. Domain decomposition and diagonal scaling preconditioners were investigated for parallel implementation. A formulation that includes fluid viscosity and that can simulate both pressure and shear waves in fluid was developed. An acoustic wave tube was built, tested, and shown to be an effective means of testing acoustic loading on simple test structures. The tube is capable of creating a semi-infinite acoustic field due to nonreflecting acoustic termination at one end. In addition, a micro-torsional disk was created and tested for the purposes of investigating acoustic shear wave damping in microstructures, and the slip boundary conditions that occur along the wet interface when the Knudsen number becomes sufficiently large.

Intentionally Left Blank

Contents

Nomenclature

List of symbols

A_{lm}	Modal coefficient of mode *l,m,* Pa
a	Acceleration, m/s^2
C_a	Damping matrix of fluid
C_s	Damping matrix of structure
c	Acoustic speed in air, m/s
FRF_{1a}	Frequency response function from acoustic pressure at Mic 1 to acceleration at the measured point on the structure
f	Frequency, Hz
f_{cutoff}	Cutoff frequency, Hz
j	$\sqrt{-1}$
$H^1(\Omega)$	Sobolov space of order 1
K_a	Stiffness matrix of fluid
K_s	Stiffness matrix of structure
k	Wave number = w/c, m^{-1}
k_z	Wave number in z direction, m^{-1}
l	Number of half-waves in x direction
M_a	Mass matrix of fluid
M_s	Mass matrix of structure
m	Number of half-waves in y direction
L_x	Inner dimension of tube in horizontal direction, m
L_y	Inner dimension of tube in vertical direction, m
L_z	Length of tube, m
P_0	Amplitude of acoustic pressure, Pa
P_i	Complex amplitude of incident wave, Pa
P_{mic}	Sound pressure at microphone, Pa
P_r	Complex amplitude of reflected wave, Pa
P_t	Complex amplitude of transmitted wave, Pa
p	Acoustic pressure, Pa
p_i	Acoustic pressure due to incident wave, Pa
p_r	Acoustic pressure due to reflected wave, Pa
S	Cross-section area of tube, m^2
S_{11}	Auto-spectrum of acoustic pressure at Mic 1
S_{12}	Cross-spectrum of acoustic pressures at Mic 1 and Mic 2
S_{13}	Cross-spectrum of acoustic pressures at Mic 1 and Mic 3.
S_{1a}	Cross-spectrum of acoustic pressures at Mic 1 and acceleration at a measured point on the structure
T	solid/fluid coupling matrix
u	Vector of displacements of structure, m
t	Time, s
$V_{speaker}$	Voltage to loudspeaker as function of frequency, V
x	Position along the x axis in the tube, m
μ_o	coefficient of shear viscosity
μ_{uo}	coefficient of bulk viscosity
y	Position along the y axis in the tube, m
Z_L	Impedance of termination, N/(m/s)
z	Position along the tube, m
z_i	Position of microphone number-i, m
z_{plate}	Position of plate, m
ϕ	Velocity potential of acoustic fluid
ρ	Density of air, kg/m^3
ω	Radial frequency, rad/s
Ω_s	Physical domain of solid/structure
Ω_f	Physical domain of fluid
$\partial\Omega_{wet}$	"Wet" interface between solid and fluid

1.0 Introduction

Coupled acoustical-structural interactions are commonly found in many engineering systems of interest to the weapons community. A few common applications include prediction of structural damage of payloads due to intense acoustic fields during launch, vibrations of electronic packages due to sounds from jet engines and aerodynamic boundary layers, acoustic radiation damping in MEMS[1], noise radiation from tires, and many other applications. These applications drive the need for predictive simulation capabilities and experimental investigations.

Two separate finite element formulations for the coupled structural acoustics problem were developed in this project. The first involved an acoustic potential(scalar)-based method, while the second was an acoustic vector-based method. In both cases the structural equations were solved in terms of displacement. For the latter approach, the research areas were to include viscosity and shear effects into the formulation. Commercial acoustics codes neglect fluid viscosity and thus cannot simulate shear waves in fluid. These waves can lead to significant structural dissipation, especially in MEMS. For the potential-based method, the main area of research was the massively parallel implementation.

Massively parallel implementation is still an active area of research in coupled structural acoustics. Massively parallel simulations are essential in structural acoustic computation, since they allow for the possibility of large numbers of degrees of freedom in the models. Infinite and semi-infinite acoustic fields, which are present in all of the applications listed above, require a large number of elements, and in frequency domain computations the number of required degrees of freedom rapidly increases with frequency. Thus, in order to solve realistic structural acoustic problems, massively parallel computations are an integral part.

Two experimental investigations were also carried out as part of this project. First, an acoustic wave tube was designed and built for the purposes of macroscale acoustic experiments. In order to simulate semi-infinite fields, one end of the tube was fitted with a built-in anechoic termination, while the other had a loudspeaker for excitation. A new procedure was developed for experimental modal analysis using acoustic (i.e. non-contact) excitation. A simple case with structural-acoustic interaction was modeled with the acoustic formulations developed in this project, and compared with the experimental results. A laboratory test was done on a corresponding structure in the tube. As will be shown in later sections, the agreement between the model and the test results was very good.

Second, in order to observe the effect of acoustic shear wave dissipation on a MEMS structure, a prototypical microdisk was designed and tested. A torsional spring was mounted to the disk, which rested above a flat planar surface. Given an initial angular rotation, the disk was allowed to freely oscillate in torsion until the amplitude of

[1] MEMS, or micro electro mechanical systems, are typically a few hundred micrometers in dimension. With these small dimensions, air damping becomes very important.

oscillation had decayed below a predefined level. In this case, no pressure waves were created in the fluid and the acoustic response consisted only of shear waves. In this way, the effect of acoustic shear wave dissipation was isolated.

2.0 Finite Element Methods for Structural Acoustics

2.1 Spatial Discretization Techniques

Spatial discretization techniques for structural acoustics can be divided into two groups: potential (scalar)-based methods, and vector-based methods. In the former case, the potential could be represented as pressure, velocity potential, or displacement potential. In the latter case, a vector wave equation is used for the fluid, and it could be in terms of either fluid displacement or fluid velocity.

The mathematical formulations for the vector-based methods suffer from the presence of spurious zero energy rotational modes in the fluid, and this is the main area of research for these methods. The formulations for the potential-based methods are well understood, but the parallelization of the coupled structural acoustics problem with these formulations is still an area of active research.

Potential-based methods can be further classified into two and three-field formulations. In the two-field formulation, the fluid is represented in terms of the pressure, velocity potential, or displacement potential, and the structural degrees of freedom are represented as displacements (and possibly rotations for shell elements) [Everstine, 1997]. Three-field formulations [Felippa *et al.*, 1990, Morand *et al.*, 1979], wherein the structure is also represented in terms of displacements but the fluid is modeled using a mixed formulation of pressure and displacement potential, have the advantage of matrix symmetry, with the disadvantage of a larger system of equations. Although all of these formulations are mathematically equivalent, they have different numerical properties, especially in the parallel setting.

The three-field formulations were originally developed for interior problems, i.e. elastic structures having internal cavities filled with fluid [Felippa *et al.*, 1990, Morand *et al.*, 1979]. In these formulations, no damping terms were involved. A later work [Pinsky, 1989] extended these formulations to *exterior* problems using the simplest possible exterior boundary condition, i.e. the first order Sommerfeld condition. When used in the context of the (mixed) three-field formulation, this resulted in higher order (i.e. higher than 2^{nd} order) systems of equations, rather than the standard second order system of equations that is typical of two-field formulations. This is undesirable, since most time integrators (Newmark beta and alpha methods) in structural mechanics are based on second order systems. Also, higher order systems of equations of this type would require special solvers for eigenanalysis. Thus, the current state of the art of three-field formulations for structural acoustics appears to be focused on interior problems, with limited results for exterior problems.

The vector approach consists of discretizing a vector wave equation for the fluid, rather than the standard scalar wave equation [Bermudez *et al.,* 1994, Hamdi *et al.,* 1978, Chen *et al.,* 1990, Wilson *et al.,* 1983]. This approach has the advantage of leading to symmetric, positive (semi) definite linear systems (for the time-domain), but the disadvantage of a large null space. These spurious modes can be eliminated either with the introduction of a penalty term, or with the use of Raviert-Thomas elements [Bermudez *et al.,* 1994]. An additional approach is to include viscosity in the formulation. This approach is described in this report. By including viscosity in the vector formulation, both shear and pressure waves in the fluid can be simulated. In many applications (especially MEMS), acoustic shear waves in fluid lead to significant energy dissipation and thus must be accommodated.

The governing equations of acoustics and coupled structural acoustics vary depending on the formulation used for the fluid. For the structure, the unknown is almost always displacement. The fluid is always assumed to be compressible. If viscosity and or thermal conductivity are to be included, the equations of acoustics can be derived from a linearization of the Navier Stokes equations [Aldridge, 2002]. When viscosity and thermal conductivity are neglected, the acoustic equations can be derived from a linearization of the isentropic Euler equations. In either case, one obtains a system of first order hyperbolic partial differential equations. These equations can be combined to form wave equations, which are then discretized with the finite element method to obtain semi-discrete equations of motion. More on this will be given in the following sections.

2.1.1 Compressible, inviscid fluid

For the isentropic, invicsid fluid, the governing equations for fluid and solid (assuming second order equations of motion for the solid, and a scalar wave equation for the fluid) are

$$\begin{aligned} r_s u_{tt} - \nabla \bullet s &= f \qquad \Omega_s x[0,T] \\ \frac{1}{c^2} f_{tt} - \Delta f &= 0 \qquad \Omega_f x[0,T] \end{aligned} \tag{1}$$

for the solid and fluid, respectively. Here f corresponds to the velocity potential of the fluid, and u corresponds to the displacement of the structure. The speed of sound in fluid is denoted by c. The subscripts ‘s’ and ‘f’ refer to solid and fluid, respectively. We note that, at this point, the equations of motion for the structure in equation 1 are written in the most general form, which could include both material and geometric nonlinearities. Later these will be specialized to the linear elasticity equations. The equations of motion of the fluid are written in the form of a linear wave equation, which assumes linear constitutive behavior of the fluid. Using the theory of *nonlinear acoustics,* one can construct wave equations that are nonlinear and that account for such nonlinearities in fluid [Blackstock, 1998]. In this report nonlinear acoustics will not be addressed. The boundary conditions on the fluid/solid interface (wet interface, which is designated by $\partial\Omega_{wet}$), are

$$\frac{\partial f}{\partial n} = -r_f \dot{u}_n \qquad \text{on } \partial\Omega_{wet} x[0,T]$$
$$s_n = -\dot{f} \tag{2}$$

These correspond to continuity of velocity and stress on the wet interface. Thus far we have assumed homogeneous (i.e. zero) initial conditions for the structural displacement and fluid velocity potential, and their corresponding velocities. This is usually the case, and thus we do not address those details here.

The weak formulation of the coupled problem is constructed by multiplying the two partial differential equations in equation 1 by test functions, and integrating by parts. This results in the following weak formulation.

Find the mapping $(u, f) \qquad [0,T] \to \left(H^1(\Omega_s)\right)^3 x H^1(\Omega_f)$ such that

$$\begin{aligned} r\langle u_{tt}, w\rangle + \langle s, \nabla^s w\rangle - \int_{\partial\Omega_{wet}} \frac{\partial s}{\partial n} w &= \langle f, w\rangle + \int_{\partial\Omega_n} gw \qquad \Omega_s \\ \frac{1}{c^2}\langle f_{tt}, y\rangle + \langle \nabla f, \nabla y\rangle + \int_{\partial\Omega_{wet}} \frac{\partial f}{\partial n} y &= 0 \qquad \Omega_f \end{aligned} \tag{3}$$

$\forall w \in \left(H^1(\Omega_s)\right)^3$ and $\forall y \in H^1(\Omega_s)$,

where $\partial\Omega_n$ is the portion of the solid/structural boundary that has applied loads, which are denoted by g. Also, $\nabla^s = \frac{1}{2}\left(\nabla + \nabla^T\right)$ is the symmetric part of the gradient operator. We note that, if Dirichlet boundary conditions were applied to part of the structure, or if the fluid had a portion of its boundary subjected to Dirichlet conditions, then the Sobolov spaces $\left(H^1(\Omega_s)\right)^3$ and $H^1(\Omega_s)$ would be modified accordingly to correspond to spaces that have those same boundary conditions. We also note that in the integration on the wet interface, the normal is defined to be positive going from solid into the fluid. This results in the difference in sign in the two wet interface integrals in equation 3. Inserting the boundary conditions from equation 2, we obtain the formulation

Find the mapping $(u, f) \qquad [0,T] \to \left(H^1(\Omega_s)\right)^3 x H^1(\Omega_f)$ such that

$$\begin{aligned} r\langle u_{tt}, w\rangle + \langle s, \nabla^s w\rangle + \int_{\partial\Omega_{wet}} \dot{f} w &= \langle f, w\rangle + \int_{\partial\Omega_n} gw \\ \frac{1}{c^2}\langle f_{tt}, y\rangle + \langle \nabla f, \nabla y\rangle - r_f \int_{\partial\Omega_{wet}} \dot{u}_n y &= 0 \end{aligned} \tag{4}$$

$\forall w \in \left(H^1(\Omega_s)\right)^3$ and $\forall y \in H^1(\Omega_s)$.

Inserting the spatial discretizations $u = \sum u_i g_i$ and $f = \sum f_i g_i$ into equation 4 yields the following semidiscrete system of equations

$$\begin{bmatrix} M_s & 0 \\ 0 & M_f \end{bmatrix} \begin{bmatrix} \ddot{u} \\ \ddot{f} \end{bmatrix} + \begin{bmatrix} C_s & T \\ -r_f T^T & C_f \end{bmatrix} \begin{bmatrix} \dot{u} \\ \dot{f} \end{bmatrix} + \begin{bmatrix} K_s & 0 \\ 0 & K_f \end{bmatrix} \begin{bmatrix} u \\ f \end{bmatrix} = \begin{bmatrix} f_s \\ f_f \end{bmatrix} \tag{5}$$

where M_s and M_f denote the mass matrices for solid and fluid, and K_s K_f denote the stiffness matrices. The coupling matrices are denoted by T and T^T. Damping in either the fluid or structure is accounted for by the damping matrices C_s and C_f. A subtle point regarding the damping terms is that C_f does *not* completely account for viscous fluid damping, since in the case of a viscous fluid the boundary conditions on the wet interface change. This will be described more fully in the next section.

This equation can be symmetrized in a number of ways. For example, the second equation can be multiplied by $\frac{-1}{r_f}$. In subsequent equations we use equations of the following form.

$$\begin{bmatrix} M_s & 0 \\ 0 & \tilde{M}_f \end{bmatrix} \begin{bmatrix} \ddot{u} \\ \ddot{f} \end{bmatrix} + \begin{bmatrix} C_s & T \\ T^T & \tilde{C}_f \end{bmatrix} \begin{bmatrix} \dot{u} \\ \dot{f} \end{bmatrix} + \begin{bmatrix} K_s & 0 \\ 0 & \tilde{K}_f \end{bmatrix} \begin{bmatrix} u \\ f \end{bmatrix} = \begin{bmatrix} f_s \\ \tilde{f}_f \end{bmatrix} \tag{5a}$$

The system is now symmetric, but the matrices are indefinite (but nonsingular).

2.1.2 Compressible, viscous fluid

Dissipative mechanisms in the fluid, such as viscous loss or heat transfer, fall into the category of *absorption theory* for acoustics [Temkin, 1981]. In the case of a viscous, non-heat conducting fluid the equations of motion of the fluid can be represented in terms of a viscous, vector wave equation. The governing equations, in terms of fluid displacement, are

$$u_{tt} - c^2 \nabla(\nabla \bullet u) - u_o \nabla^2 u_t + \frac{1}{r}(m_{uo} + \frac{1}{3} m_o) \nabla(\nabla \bullet u_t) = 0 \tag{6}$$

where u is the fluid displacement, $u_o = \frac{m_o}{r}\left(1 + \frac{3}{4}\frac{m_{uo}}{m_o}\right)$, and m_o, m_{uo} are the coefficients of shear and bulk viscosity, respectively. We note that equation 6 is a vector wave equation, since it is in terms of fluid displacement, and that the latter two terms in the equation are dissipative since they involve first order derivatives in time.

Coupling equation 6 with the elasticity equations is straightforward since the unknowns in both cases are displacement. Due to the presence of viscosity, no-slip or Maxwell type of slip conditions can be applied at the wet interface. Slip boundary conditions are common in MEMS.

Multiplying by a test function and integrating by parts, using no-slip boundary conditions, and inserting the spatial discretizations, we obtain a coupled system of equations of the form

$$[M]\ddot{u} + [C]\dot{u} + [K]u = f \tag{7}$$

where M, K, and C represent the global mass, stiffness, and damping matrices, obtained by combining the element-level matrices from both fluid and solid. A distinctive difference between this equation and the coupled equations for the potential-based acoustic formulation is the absence of coupling operators in the case of equation 7. In this case the coupling from fluid to solid comes directly from the shared degrees of freedom on the wet interface, and their contributions from both the structural and acoustic element-level matrices. This is an advantage of the vector-based acoustic formulations, since the implementation need not deal with coupling matrices.

2.2 Parallel Domain Decomposition

Domain decomposition strategies for coupled structural acoustics have been investigated in [Mandel, 2001, Feng, 2000]. For the parallel case, the most common approach is that each processor has only one subdomain, and that the subdomains are connected. In that case, the most general domain partitioning scheme for coupled structural acoustics would result in each processor owning groups of elements as shown in Figure 1. On each subdomain there are four possibilities: internal fluid (type I), internal solid (type II), mixed fluid/solid (type III), and solid or fluid containing a portion of the wet interface (type IV). The first two of these present no complications, because they generate no components of a coupling matrix. If the decompositions of the fluid and solid are performed independently, subdomains of type III are not generated. In that case, only subdomains of types I, II, and IV would be present. Subdomains of type IV could be generated regardless of whether the decompositions of the fluid and structure were performed independently. Subdomains of type III are advantageous because all the coupling matrices are interior to a subdomain. The most general decompositions, as those considered in this report, contain all four types of subdomains simultaneously.

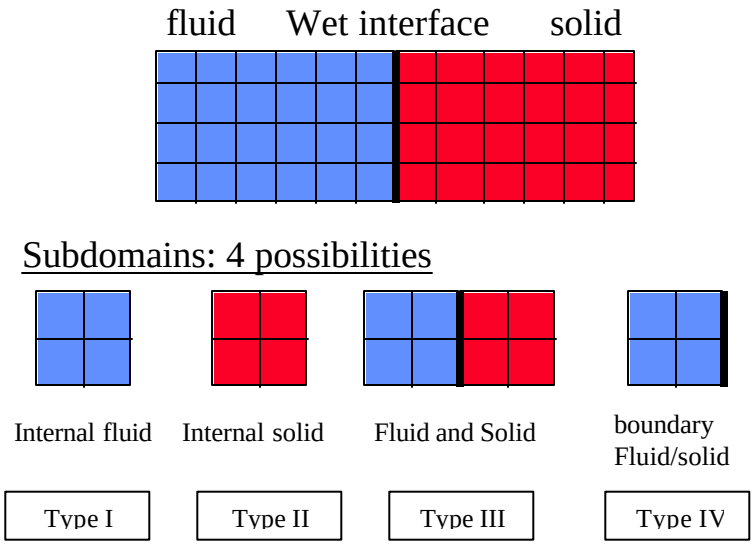

Figure 1. Parallel decomposition of the coupled problem - four possible types of subdomains

Rather than place restrictions on how the elements are structured on the subdomains, we consider all such decompositions. Allowing this arbitrary decomposition approach for the coupled problem is beneficial for many reasons. First, by allowing for arbitrary decompositions, we take the most general approach while retaining the option for more restrictive decompositions. By eliminating any of the 4 types of decompositions, we recover other approaches given in the literature. For example, by eliminating subdomains of type III, we recover the same decomposition approach that was given by [Mandel, 2001].

There are other advantages to the arbitrary decomposition approach. In many problems of interest, the fluid is fragmented into many pieces. For example, structures like the W80 and W76 have an exterior fluid as well as many interior cavities. Complex microsystems containing MEMS and surface acoustic wave (or SAW) devices may also fall into this category. The arbitrary decomposition approach allows domains like these to be decomposed in a single step, without requiring separate decompositions for the fluid and structure.

Another advantage is related to the linear solvers for the coupled problem, and subdomain aspect ratios. In this work a FETI-DP[2] solver was used for solving the coupled linear systems. FETI-type solvers have a long history, as documented in the

[2] Contact: Kendall Pierson, Sandia National Laboratories, khpiers@sandia.gov

references [Farhat, 1991, Bhardwaj et al., 2000, Farhat et al., 2000, Farhat et al., 2001]. It is well known that the convergence rates of FETI methods deteriorate in the presence of long, thin subdomains [Farhat et al., 1995]. Domains containing long, thin regions of alternating fluid and solid are common, especially in MEMS. By requiring subdomains to only have fluid or solid, the resulting domain decomposition would share the topology of long, slender pieces, and the resulting convergence rates could suffer.

Perhaps the most important reason for support of arbitrary decompositions is pragmatic. Most decomposition tools available to analysts have no capability to select between the connection types.

As an example of the arbitrary decomposition approach, structural acoustic simulations were conducted on a tire with several different numbers of processors. The goal is to demonstrate that the results obtained on the same problem but on varying numbers of processors are the same, and thus that the result is *invariant* with respect to the number of subdomains, in the presence of all four types of decompositions. For any given decomposition, only some, or all, of the four types of subdomains in Figure 1 are present. It is the invariance with respect to the presence of the four different types of subdomains that is of interest here. Table 1 shows a comparison of the 30 and 50 processor solutions, which shows effectively no difference between the two solutions.

Table 1. Comparison of solutions resulting from two arbitrary decompositions.

$\|f_{30}\|$	$\|f_{50}\|$	$\frac{\|f_{30}-f_{50}\|}{\|f_{30}\|}$	$\|u_{30}\|$	$\|u_{50}\|$	$\frac{\|u_{30}-u_{50}\|}{\|u_{30}\|}$
7.76e6	**7.76e6**	**1.13e-9**	**.205**	**.205**	**6.14e-9**

In a decomposition that only involved subdomains of types I, II, and III, the subdomain matrix assembly would be standard, and the coupling matrices would be assembled naturally in the subdomains that contain parts of the wet interface. However, including subdomains of type IV in the decomposition adds an extra complication. Since FETI-DP requires nonsingular subdomain matrices (after removal of corner degrees of freedom), the coupling matrices must be handled with care.

For the time domain, we define the dynamic matrices as

$$A_s = \frac{4}{\Delta t^2} M_s + K_s$$
$$A_f = \frac{4}{\Delta t^2} M_f + K_f \qquad (8)$$

For the frequency domain, the corresponding matrices would be

$$A_s = -\omega^2 M_s + K_s$$
$$A_f = -\omega^2 M_f + K_f \tag{9}$$

We note that these matrices are nonsingular due to the presence of the mass terms. We also note that these matrices are not the complete subdomain matrices, but are only the fluid and solid portions separated out.

The assembly of the above stiffness and mass matrices for acoustic and structural elements proceeds in the standard way. The coupling matrices (i.e. the T and T^T operators from equation 5) also assemble in the standard way if the portion of the wet surface involved in the coupling lies within the interior of the subdomain. This is true for subdomains of types I, II, and III. For subdomains of type IV, the situation is different. Since subdomains of type IV involve portions of the wet interface that are also on subdomain boundaries, the coupling matrix assembly in this case could proceed in a number of different ways, each with different consequences.

There are three options for assembling the coupling matrices for type IV subdomains. We first note that these matrices could be assembled from either the fluid or solid regions, since both regions own the degrees of freedom involved in the coupling. The first option is to assemble both T and T^T from the fluid, and the second is to assemble from the solid side. The third option would be to have the fluid elements assemble T^T and the solid elements assemble T.

We note that, when assembling both T and T^T from only one side, all of the degrees of freedom involved in coupling do not need to be active on both sides. For example, if both are to be assembled from the solid side, then there is no need to have the solid degrees of freedom active on the fluid side. Thus, in that case the continuity across subdomain boundaries would be enforced only with the Lagrange multipliers for the velocity potential. The solid degrees of freedom would then be coupled on the adjacent subdomain through the coupling operators.

We now examine the subdomain matrices for the three approaches described above. Table 2 outlines the options

Table 2. Subdomain matrices for type IV subdomains in coupled structural acoustics.

Option 1	Option 1	Option 2	Option 2	Option 3	Option 3
$\begin{bmatrix} A_f & T \\ T^T & \end{bmatrix}$	$[A_s]$	$[A_f]$	$\begin{bmatrix} A_s & T \\ T^T & \end{bmatrix}$	$\begin{bmatrix} A_f & 0 \\ T^T & 0 \end{bmatrix}$	$\begin{bmatrix} A_s & T \\ 0 & 0 \end{bmatrix}$
Singular	Nonsingular	Nonsingular	Nonsingular	Singular	Singular

As can be seen, with the requirement that the subdomain matrices be nonsingular, the only option for placing the coupling matrices is option 2. For option 2, the fluid subdomain matrix is nonsingular. The solid subdomain matrix for option 2 can be shown to be nonsingular by a simple rank argument. A similar argument can be used to show that the fluid subdomain matrix in option 1 is singular, and thus that this option is not viable.

2.3 Equation Scaling and Preconditioning

Due to the severe property mismatch between structure and fluid, the global matrices for structural acoustics typically have very poor condition numbers, thus placing a high burden on the linear solver. For the example of steel in air, the stiffness and mass ratios between solid and fluid are several orders of magnitude, and much worse than typical large material mismatch encountered in structural mechanics, such as steel next to foam. Scaling and other preconditioning procedures for FETI-DP have been documented in the literature [Farhat et al., 2000]. However, these scaling procedures have only been applied to the interface matrices, i.e. after the Schur complements on each subdomain have been completed.

A symmetric diagonal scaling procedure was recently developed for the coupled frequency response problem [Mandel, 2001]. This was different than the standard scaling for FETI-DP in that the scaling was applied to the subdomain matrices directly rather than to the interface matrices. However, this procedure involved scaling of both the subdomain matrices as well as the matrices corresponding to Lagrange multipliers. Since the Lagrange multiplier matrices are typically not stored, scaling them can be difficult.

An additional scaling procedure was developed in [Day, 1999] for the purpose of using FETI-DP in parallel structural eigenvalue analysis. This procedure only required scaling the subdomain matrices. The scaling was chosen such that the Lagrange multiplier matrices were invariant to the scaling. While this procedure was only developed for the structural problem, it is possible to extend it to the coupled structural acoustics problem, provided that the subdomain matrices are defined to include the coupling operators. More will be given on this in the following paragraphs.

If we consider the extended linear system corresponding to a FETI-DP domain decomposition, and then apply symmetric diagonal scaling on that extended system, we have

$$\begin{bmatrix} A & B^T \\ B & 0 \end{bmatrix}\begin{bmatrix} u \\ l \end{bmatrix} = \begin{bmatrix} f \\ 0 \end{bmatrix} \Leftrightarrow \begin{bmatrix} D_1 & 0 \\ 0 & D_2 \end{bmatrix}\begin{bmatrix} A & B^T \\ B & 0 \end{bmatrix}\begin{bmatrix} D_1 & 0 \\ 0 & D_2 \end{bmatrix}\begin{bmatrix} D_1^{-1}u \\ D_2^{-1}l \end{bmatrix} = \begin{bmatrix} D_1 f \\ 0 \end{bmatrix} \qquad (10)$$

where the Lagrange multipliers l enforce continuity across subdomains, and the diagonal matrices D_1 are chosen such that the diagonal entries of D_1AD_1 are unity for degrees of freedom that are internal to a subdomain. For shared degrees of freedom, the diagonal entries of D_1 are chosen so that the corresponding diagonal entries of D_1AD_1 are as close as possible to unity. We note that there are also corner points in the decomposition where the inter-subdomain continuity is satisfied exactly, and thus in reality equation 10 corresponds to a 3x3 partition rather than a 2x2 partition. However, a 2x2 is sufficient to illustrate the scaling procedure.

As shown in [Day, 1999], if the scaling matrices are chosen such that $D_1B^T D_2 = B^T$, then we see that the 'B' matrices corresponding to Lagrange multipliers do not need to be scaled. This greatly simplifies the solver implementation.

The scaling procedure in [Day, 1999] was developed for the structural eigenanalysis problem. In order to apply this procedure to the coupled structural acoustic problem, we must include the coupling matrices in the scaling procedure. To demonstrate this, we write the full system as

$$\begin{bmatrix} A_s & T & B_s^T & 0 \\ T^T & -A_f & 0 & B_f^T \\ B_s & 0 & 0 & 0 \\ 0 & B_f & 0 & 0 \end{bmatrix}\begin{bmatrix} u \\ f \\ l_s \\ l_f \end{bmatrix} = \begin{bmatrix} f_s \\ f_f \\ 0 \\ 0 \end{bmatrix} \qquad (11)$$

where now the linear system involves unknowns for both the structural and acoustic unknowns, as well as Lagrange multipliers for these unknowns.

In order to reduce this to the form in equation 10, we group the terms as follows

$$\begin{bmatrix} \begin{bmatrix} A_s & T \\ T^T & -A_f \end{bmatrix} & \begin{bmatrix} B_s^T & 0 \\ 0 & B_f^T \end{bmatrix} \\ \begin{bmatrix} B_s & 0 \\ 0 & B_f \end{bmatrix} & \begin{bmatrix} 0 & 0 \\ 0 & 0 \end{bmatrix} \end{bmatrix}\begin{bmatrix} u \\ f \\ l_s \\ l_f \end{bmatrix} = \begin{bmatrix} f_s \\ f_f \\ 0 \\ 0 \end{bmatrix} \Leftrightarrow \begin{bmatrix} \tilde{A} & \tilde{B}^T \\ \tilde{B} & 0 \end{bmatrix}\begin{bmatrix} \tilde{u} \\ \tilde{l} \end{bmatrix} = \begin{bmatrix} \tilde{f} \\ 0 \end{bmatrix} \qquad (12)$$

where

$$\tilde{A} = \begin{bmatrix} A_s & T \\ T^T & -A_f \end{bmatrix},\ \tilde{B} = \begin{bmatrix} B_s & 0 \\ 0 & B_f \end{bmatrix},\ \tilde{u} = \begin{bmatrix} u \\ f \end{bmatrix},\ \tilde{f} = \begin{bmatrix} f_s \\ f_f \end{bmatrix}, \text{and } \tilde{l} = \begin{bmatrix} l_s \\ l_f \end{bmatrix}.$$

With this grouping, we see that the coupled problem has the same form as in equation 10, and thus the same scaling procedure can be applied, provided that the coupling matrices are included in the scaling. In the transient case the matrix to be scaled is

$$\tilde{A} = \begin{bmatrix} \frac{4}{\Delta t^2} M_s + K_s & T \\ T^T & -\frac{4}{\Delta t^2} M_f - K_f \end{bmatrix} \tag{13}$$

This implies that, with the 2x2 grouping implied in the above equations, we can apply the same scaling procedure to the coupled structural acoustics problem. Note that the equation $\tilde{A} = \begin{bmatrix} A_s & T \\ T^T & A_f \end{bmatrix}$ involves not only the matrices A_s and A_f, but also the coupling terms T and T^T. Thus, in applying the scaling to the overall linear systems, we have to scale the coupling matrices as well. We thus define the scaling procedure for the coupled problem as

$$\begin{bmatrix} \tilde{A} & \tilde{B}^T \\ \tilde{B} & 0 \end{bmatrix} \begin{bmatrix} \tilde{u} \\ \tilde{l} \end{bmatrix} = \begin{bmatrix} \tilde{f} \\ 0 \end{bmatrix} \Leftrightarrow \begin{bmatrix} D_1 & 0 \\ 0 & D_2 \end{bmatrix} \begin{bmatrix} \tilde{A} & \tilde{B}^T \\ \tilde{B} & 0 \end{bmatrix} \begin{bmatrix} D_1 & 0 \\ 0 & D_2 \end{bmatrix} \begin{bmatrix} D_1^{-1} \tilde{u} \\ D_2^{-1} \tilde{l} \end{bmatrix} = \begin{bmatrix} D_1 \tilde{f} \\ 0 \end{bmatrix} \tag{14}$$

We note that in the case of transient analysis, the right hand side must also be scaled by the diagonal matrix D_1. Also, after solving the linear system the structural and acoustic degrees of freedom must be scaled by D_1 in order to recover the final solution.

Scaling the equations of course means that we are not solving all the variables to the original accuracy. In the case of a very compliant fluid and a stiff structure, this may mean that the relative structural solution accuracy has been reduced. However, this is indeed the right thing to do. Otherwise, failure to scale the solution, and inexact iterative solves can result in meaningless results in the fluid region.

Figure 2 contains results from a simulation of a transient plane wave scattering from an elastic sphere, after applying symmetric diagonal scaling to the coupled linear system. For this simulation, 250 time steps were carried out. At later time steps, the number of iterations required for convergence to a fixed tolerance decreased significantly, due to the multiple right hand side capability in FETI-DP.

Finally, we present some graphical results from two sample problems. The first involves scattering of a plane wave on an elastic sphere. The second involves acoustic radiation from a tire. Figures 3 and 4 show the results for the two cases. The isocontours of velocity potential are shown around the sphere in Figure 3, and in the case of the tire the velocity potential around the tire is indicated by the amplitude of the xy plot above the

tire.

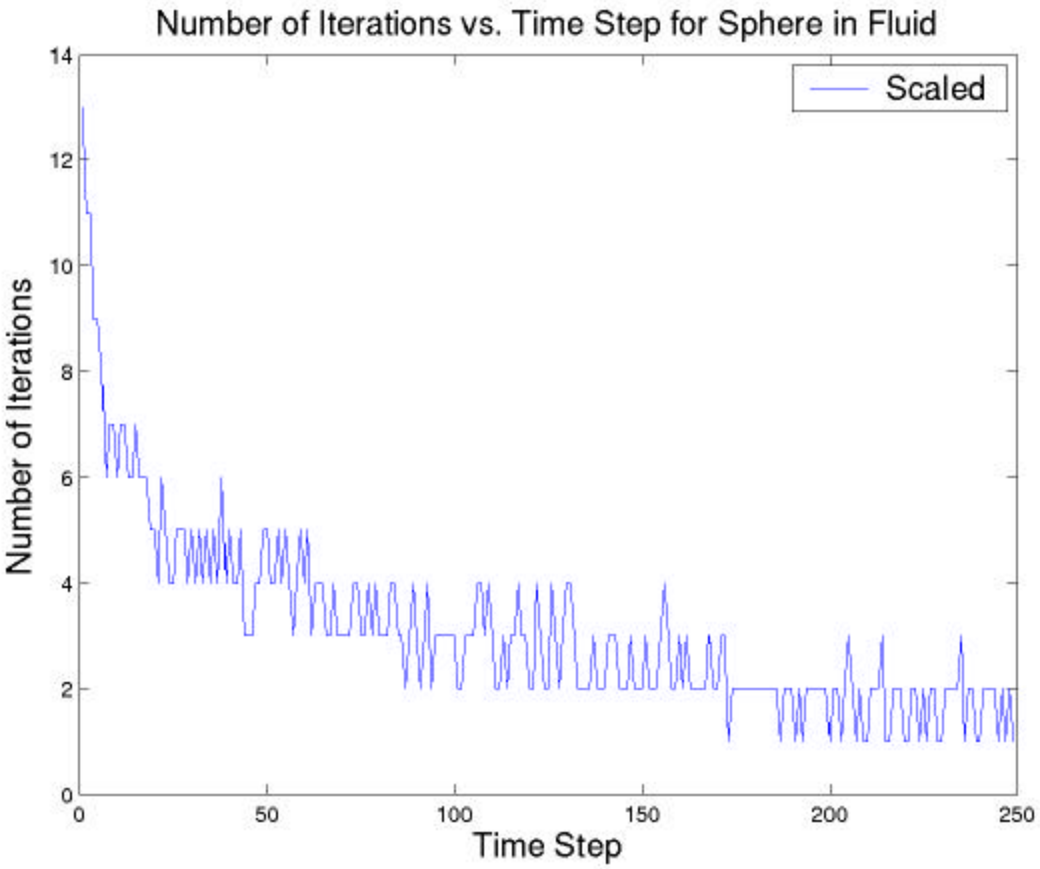

Figure 2. Acoustic scattering of plane wave on elastic sphere. The number of iterations required for convergence, with symmetric diagonal scaling.

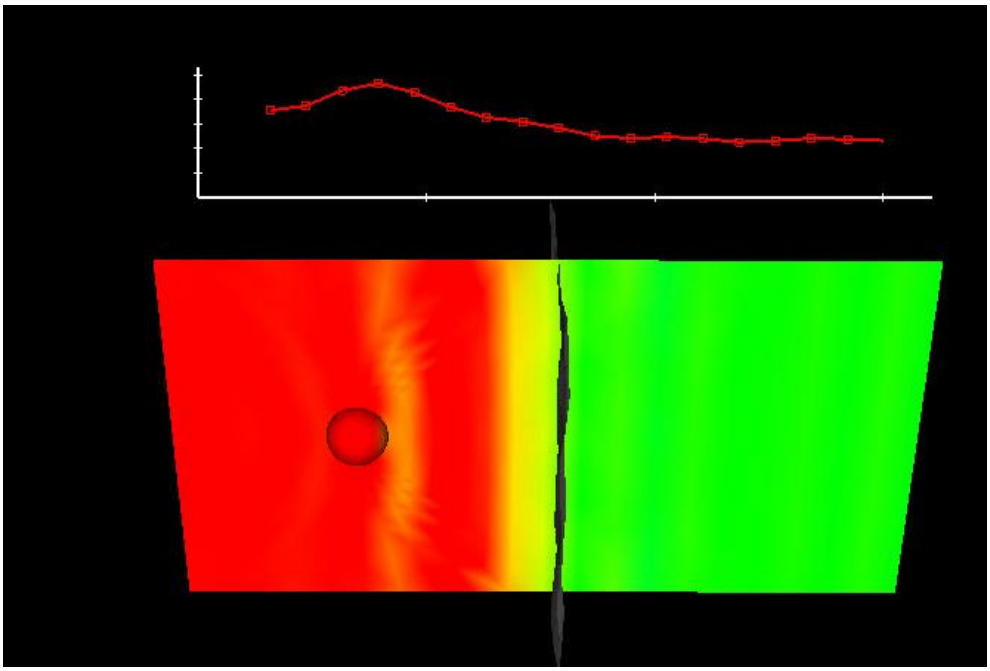

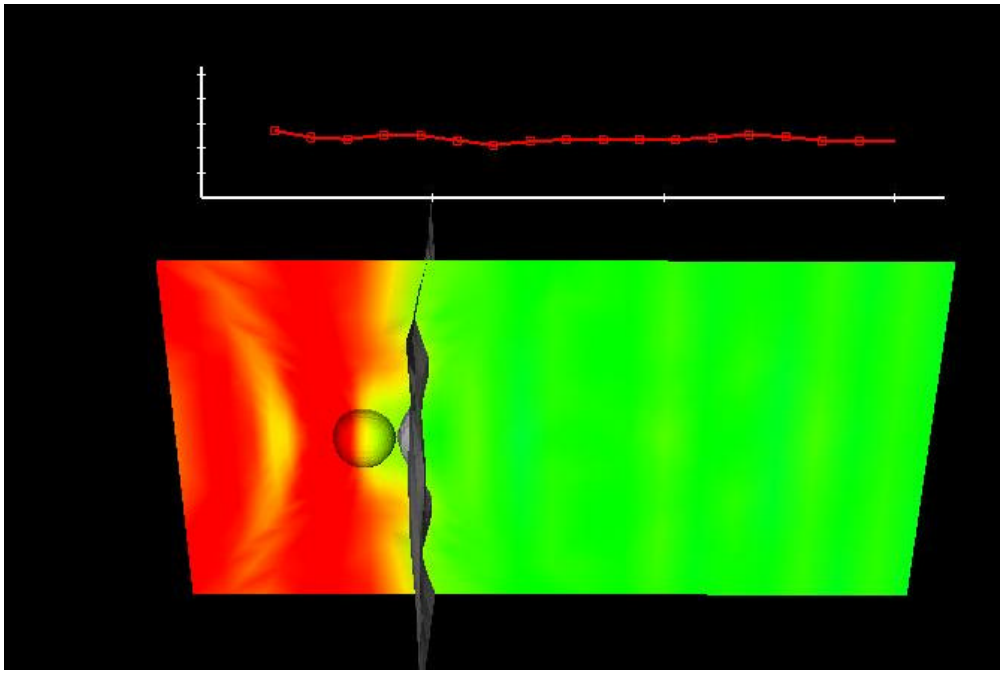

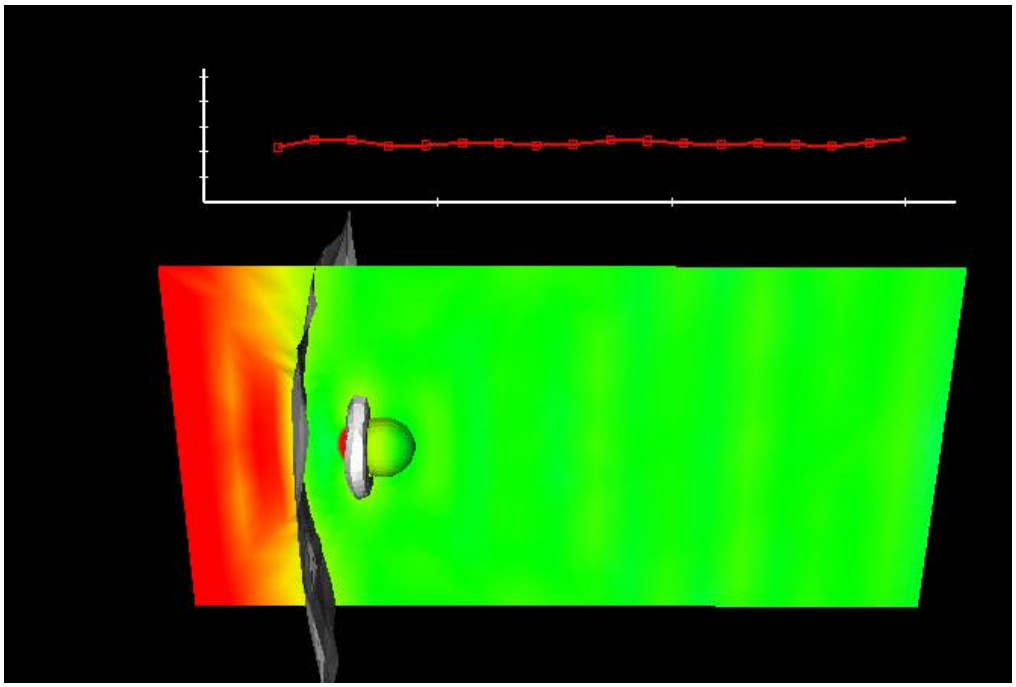

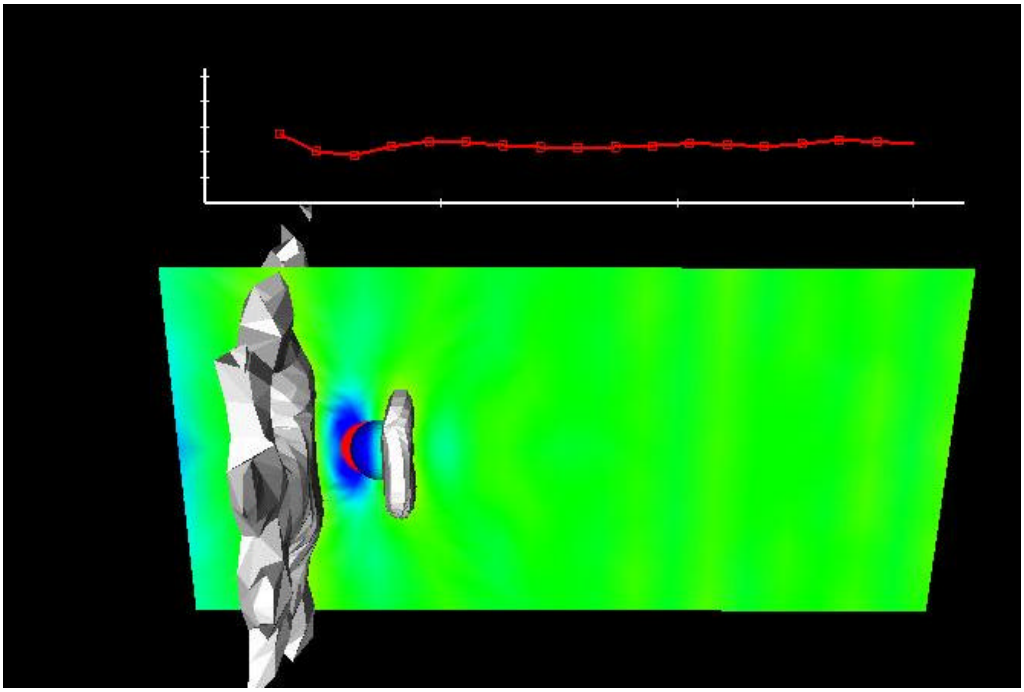

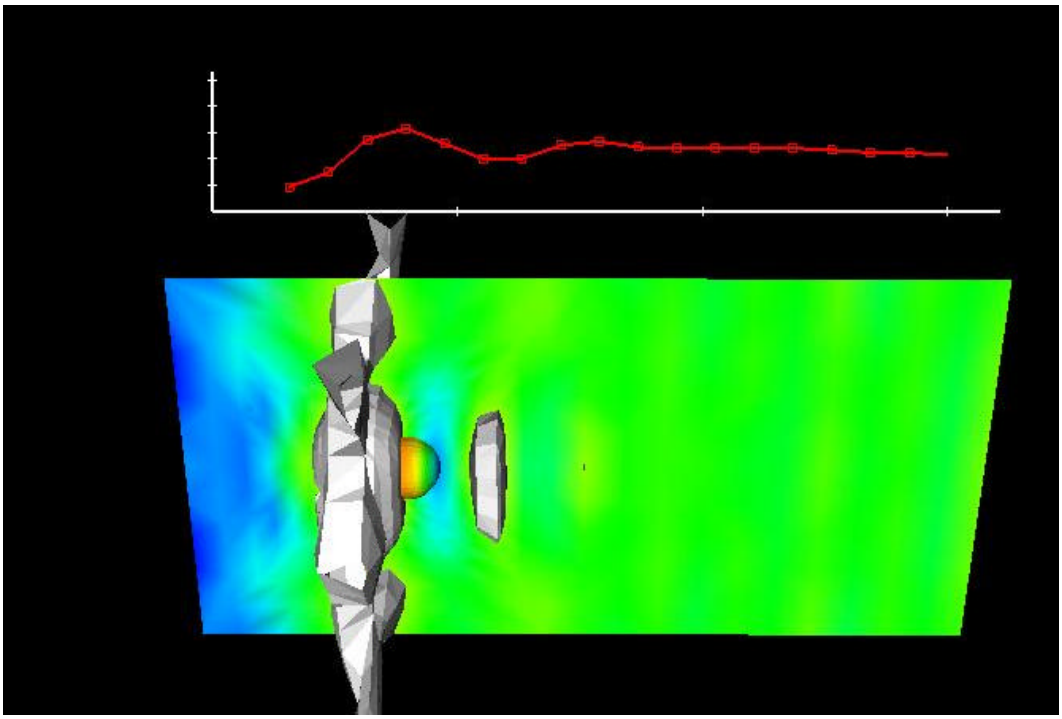

Figure 3. Scattering of acoustic wave on Elastic Sphere. Isocontours (in grey) are shown. Velocity potential shown in (top) xy plot.

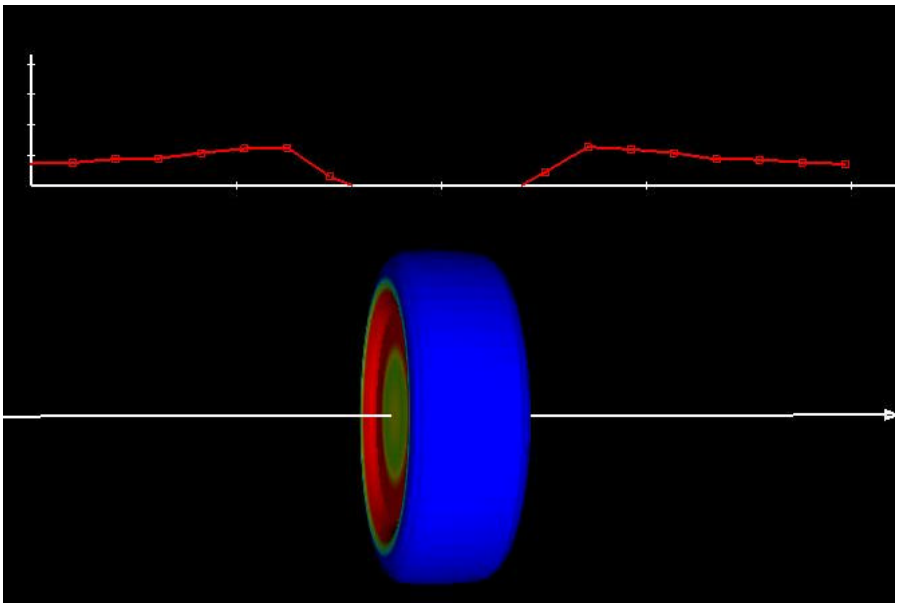

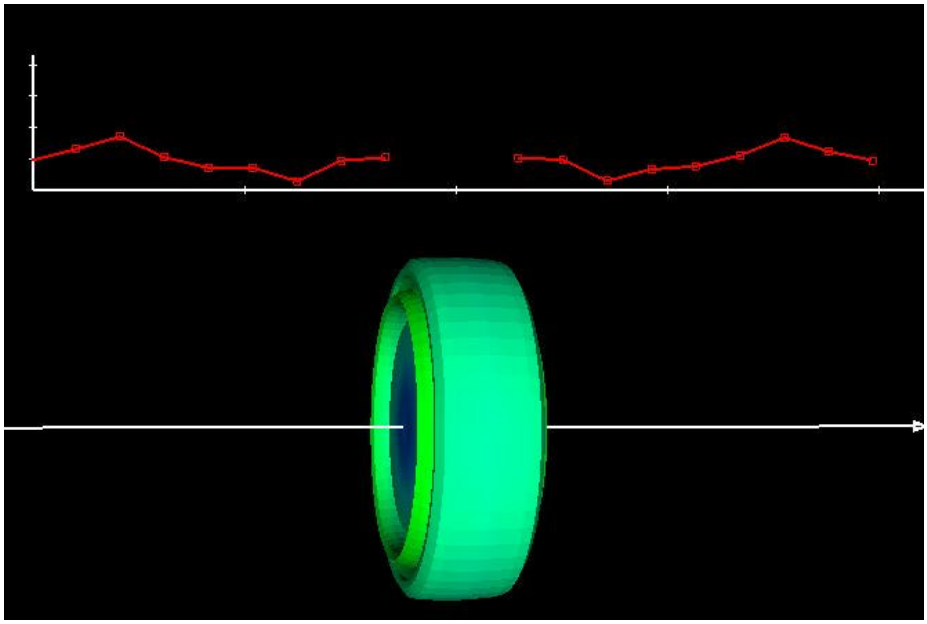

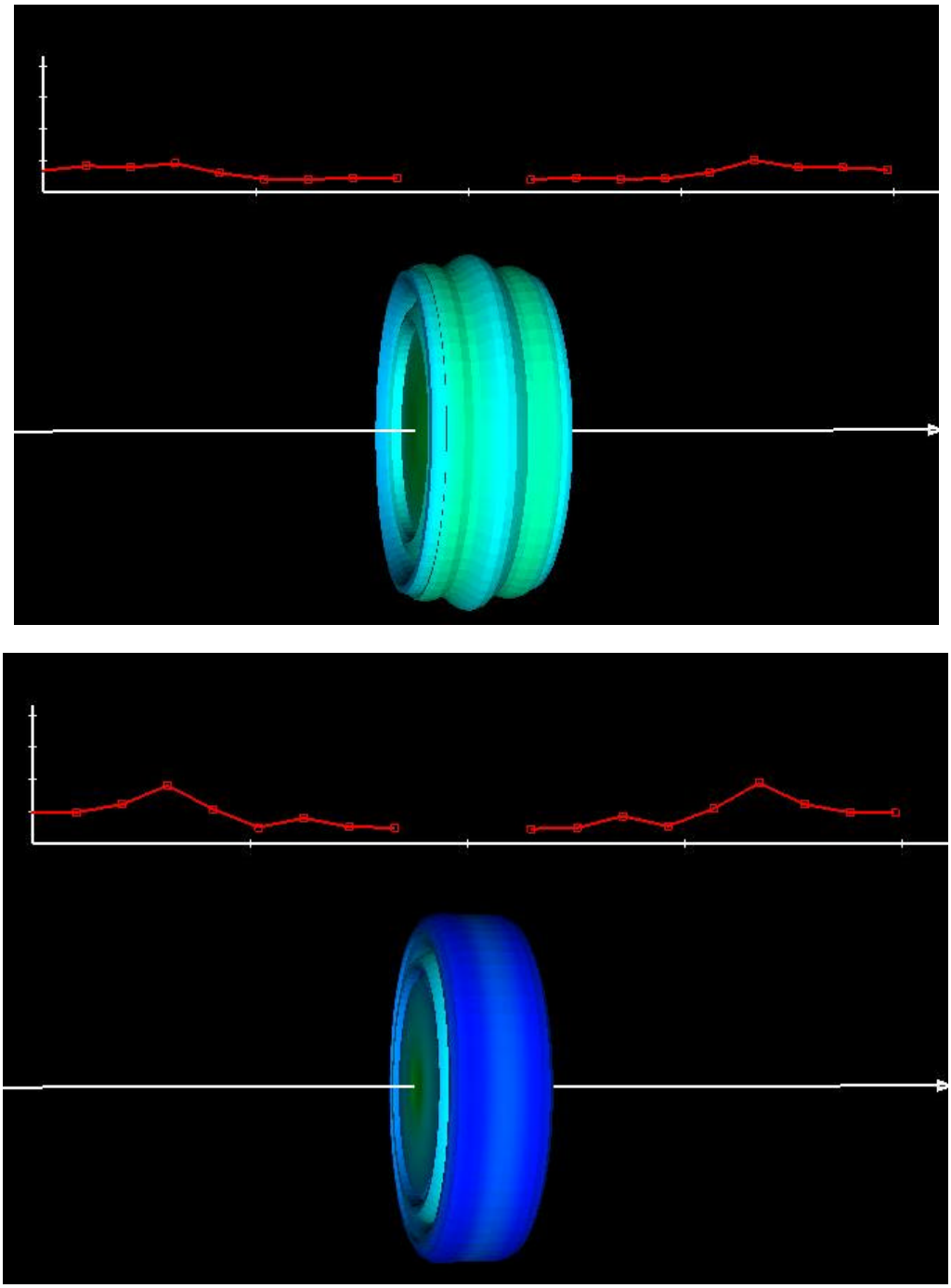

Figure 4. Coupled acoustic/structural simulation of a tire in air. Velocity potential is shown in (top) xy plot.

3.0 Planar Wave Tube for Validating Structural Acoustic Simulation

Background
Experimental validation of structural acoustic simulations requires experiments that can be modeled accurately. The wave tube described in Figure 5 is intended to provide such experiments. Specifically, the tube provides

- A well-defined test volume that can be controlled and modeled accurately around the test object.
- A traveling plane wave $p_i = P_i\, e^{-jkz}$ that can be generated, measured, and modeled accurately.
- Shielding from external noise.
- Simple, low-cost construction.

Structural acoustic experiments that can be done in the tube can be modeled accurately with Salinas. For example, a planar traveling wave generated by the speaker in combination with the tube excites a test object. The dynamic responses of the test object are measured and analyzed, as is the acoustic pressure field around the test object. These types of experiments can be modeled and simulated with the acoustic formulations described in the previous section. Agreement between the measured responses and the simulation results can be used as validation of the model and the code. Without the tube, it would be difficult to create an experimental condition that can be modeled and simulated accurately with finite element codes.

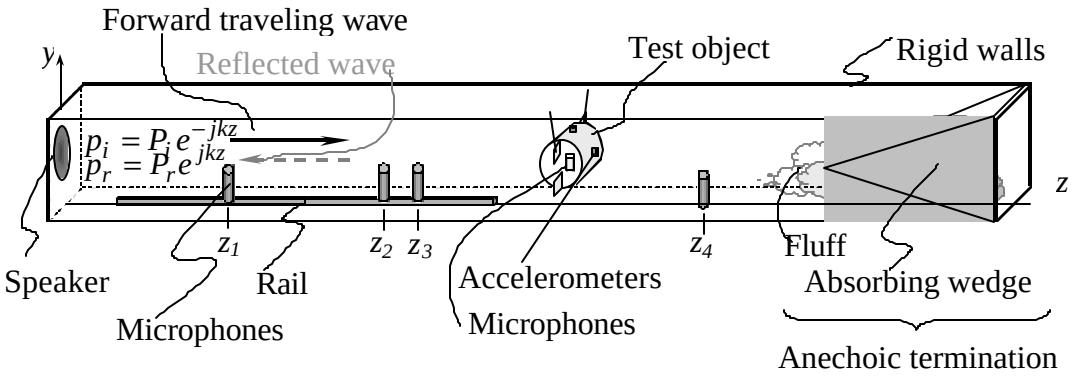

Figure 5. Sketch of wave tube (not to scale).

Principles of Operation
The principles of operation of the planar wave tube are
1) Generation of planar wavefronts, and 2) Separation of acoustic pressures into measurable forward-traveling waves and backward traveling waves. The first will be discussed later. The second is explained below. Suppose that an incident harmonic planar wave

$$p_i(z,t) = P_i e^{-jkz} e^{jwt}; z > 0 \tag{15}$$

travels forward down the tube. Reflections in the z direction causes a backward-traveling wave

$$p_r(z,t) = P_r e^{jkz} e^{jwt}; z > 0 \tag{16}$$

The acoustic pressures sensed by the microphones are the sum of the forward traveling wave pressure and the backward-traveling ("reflected") wave pressure. Measurement of the amplitudes of the forward-traveling and backward traveling waves requires two microphones and a simple calculation shown below. The acoustic pressure sensed by a microphone called Mic 2, positioned at $z = z_2$, is

$$p(z_2) = P_i e^{-jkz_2} e^{jwt} + P_r e^{jkz_2} e^{jwt} \tag{17}$$

and the acoustic pressure sensed by another microphone, called Mic 3, positioned at $z = z_3$, is

$$p(z_3) = P_i e^{-jkz_3} e^{jwt} + P_r e^{jkz_3} e^{jwt} \tag{18}$$

The above two equations can be solved for the forward-traveling incident wave amplitude

$$P_i = \frac{e^{jkz_3} p(z_2) - e^{jkz_2} p(z_3)}{2j \sin\left(k(z_3 - z_2)\right)} \tag{19}$$

and the backward-traveling wave amplitude

$$P_r = \frac{e^{-jkz_3} p(z_2) + e^{-jkz_2} p(z_3)}{2j \sin\left(k(z_3 - z_2)\right)} \tag{20}$$

As a device for validating structural-acoustic finite element calculations, the tube can be used to measure frequency response functions from the forward-traveling wave to acceleration at a point on the structure.

Design

The walls of the tube are made of 25.4 mm thick plywood. The dimensions of the inside of the tube are as follows:

Length L_z = 7.23 m, dimension in the y (vertical) direction L_y = 0.3048 m (12 in.), dimension in the x (horizontal) direction L_x = 0.3556 m (14 in.). The tube is operated in 20^o C air, where the acoustic speed is c = 332 m/s. A loudspeaker at the source end of the tube generates excitation sounds. Microphones are mounted on a traverse. The test object to be measured must fit into the cross section, and can be mounted on elastic chords from

outside the tube. The other end of the tube is closed with an anechoic termination pyramid made of sound absorbing fiber framed in wire.

Non-Planar Modes, Their Cutoff Frequencies, and Their Decaying Ranges

The most important requirement for the tube is that around the microphones it has only *planar* waves. Waves that are known to be planar are easy to model accurately, and are non-dispersive, allowing waveforms to travel down the tube with no distortion. Non-planar waves exist in the tube in practice. Mode (*m*,*n*) has *m* half-cosines along the *x*-direction and *n* half-cosines in the *y*-direction. Mode (0,0) is a plane wave, which means that in any cross section of the tube the pressure wave is uniform over the entire cross-section.

If the tube acts as a wave guide where waves travel in only one direction, then the acoustic pressure as a function of spatial coordinates and time is the real part of the following equation (Kinsler *et al.*, 1982)

$$p(x,y,z,t) = \sum_{m=0}^{\infty}\sum_{l=0}^{\infty} A_{lm}\cos\left(\frac{lp}{L_x}x\right)\cos\left(\frac{mp}{L_y}y\right)\exp\left[j\left(wt - \sqrt{\left(\frac{w}{c}\right)^2 - \left(\frac{lp}{L_x}\right)^2 - \left(\frac{mp}{L_y}\right)^2}\,z\right)\right] \tag{21}$$

where the *modal coefficients* A_{lm} are determined by the excitation from the speaker as a boundary condition. The contribution of mode (*l*,*m*) = (0,0) to the acoustic pressure field is

$$p_{0,0}(x,y,z,t) = A_{00}e^{-j(w/c)z}e^{jwt} \tag{22}$$

Since $p_{0,0}$ does not depend on *x* or *y*, the spatial distribution of mode (0,0) is constant over the cross section of the tube. Thus, mode (0,0) is termed the *planar mode*. In equation 21, the *wavenumber in the z direction*,

$$k_z(l,m) = \sqrt{(w/c)^2 - (lp/L_x)^2 - (mp/L_y)^2} \tag{23}$$

determines the propagation of mode (*l*,*m*) down the tube. At low frequencies $w < c\sqrt{(lp/L_x)^2 + (mp/L_y)^2}$, the spatial variation of $p_{l,m}$ along the *z* direction is

$$\exp\left(-j\sqrt{\left(\frac{w}{c}\right)^2 - \left(\frac{lp}{L_x}\right)^2 - \left(\frac{mp}{L_y}\right)^2}\,z\right) = \exp\left(-\sqrt{\left(\frac{lp}{L_x}\right)^2 + \left(\frac{mp}{L_y}\right)^2 - \left(\frac{w}{c}\right)^2}\,z\right) \tag{24}$$

which is an exponentially decaying function of z. This means that, at frequencies lower than $f_{cutoff}(l,m)$, mode (l,m) will decay exponentially. Numerical examples will show that the decay is within a short distance from the speaker. A non-planar mode ($l>0, m>0$) will travel far in the tube only at frequencies higher than the cutoff frequency $f_{cutoff}(l,m)$. The cutoff frequency of mode (l,m) is the lowest frequency at which the wavenumber is real. In Hz,

$$f_{cutoff}(l,m) = \frac{c}{2}\sqrt{(l/L_x)^2 + (m/L_y)^2} \tag{25}$$

To allow only planar waves to travel in the tube, the tube must be excited at frequencies lower than the cutoff frequency of the lowest non-planar mode. Based on the tube dimensions discussed here, mode (0,1) has a cutoff frequency of 467 Hz. The cutoff frequencies of the first 18 modes are shown in Table 3.

Table 3 Cutoff frequencies of tube.

Mode sequence	0	1	2	3	4	5	6	7	8
Mode number	0,0	0,1	1,0	1,1	0,2	1,2	2,0	2,1	0,3
Cutoff freq, Hz	0	466.8	544.6	717.3	933.6	1081	1089	1185	1400

Mode sequence	9	10	11	12	13	14	15	16	17
Mode number	2,2	1,3	3,0	3,1	2,3	0,4	3,2	1,4	3,3
Cutoff freq, Hz	1435	1503	1634	1699	1774	1867	1882	1945	2152

If the speaker excites the air in the tube at a frequency above the cutoff frequency of mode l,m, then all modes with lower cutoff frequencies will travel down the tube. The wavefront of each mode travels at a *phase speed*

$$c_p(l,m) = \frac{w}{k_z(l,m)} \tag{26}$$

Figure 6 shows that the phase speed w/k_z depends on frequency, except for the planar mode (0,0) where $w/k_z = c$ for all frequencies. Also, different modes have different phase speeds. This means that if the waves have non-planar modes, the wavefront of the acoustic pressure will change shapes as it travels down the tube. Reflections from test objects in the tube, if they have components in the non-planar modes, will also be distorted as they travel in the tube. This distortion in the wavefront shapes would complicate the modeling and would require measurement of acoustic pressure at many points over each cross section. This complication is another reason why excitation of non-planar modes should be avoided. Thus, the tube should be operated with excitations with frequencies lower than the cutoff frequency of the first non-planar mode.

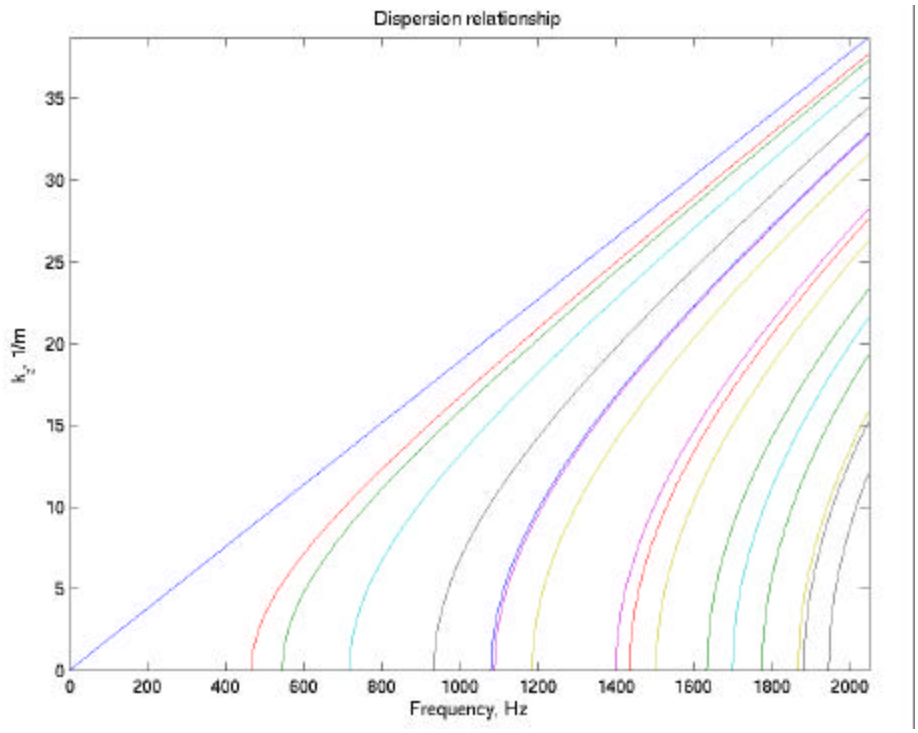

Figure 6. Relationship between wavenumber and frequency for the first 17 modes.

Even when the excitation frequency is below the cutoff frequency of the first non-planar mode, the waves traveling down the tube are planar only after a certain distance from the speaker. It is practically impossible for a speaker to produce a purely planar wave excitation at $z = 0$. In the following example, the speaker generates an acoustic pressure distribution over the cross section of the tube that can be approximated as

$$p(x,y,0,t) = \sum_{m=0}^{6}\sum_{l=0}^{6} A_{lm} \cos\left(\frac{lp}{L_x}x\right)\cos\left(\frac{mp}{L_y}y\right)\exp\left[j\left(wt - \sqrt{\left(\frac{w}{c}\right)^2 - \left(\frac{lp}{L_x}\right)^2 - \left(\frac{mp}{L_y}\right)^2}\,z\right)\right] \tag{27}$$

where the modal coefficients A_{lm} are

$$A_{lm} = \begin{cases} 0; l > 0, m > 0 \\ 0; l = 0, m \text{ is odd} \\ 0; m = 0, l \text{ is odd} \\ \dfrac{16L_y}{p^2 L_x m^2}; l = 0, m \text{ is even} \\ \dfrac{16L_x}{p^2 L_y l^2}; m = 0, l \text{ is even} \\ \dfrac{4}{L_x L_y}\left(\dfrac{L_x^2}{6} + \dfrac{L_y^2}{6} - L_x L_y\right); l = 0, m = 0 \end{cases} \tag{28}$$

(The above coefficients are from the two-dimensional Fourier cosine series expansion of the pressure distribution.) This pressure distribution is maximum at the center of the cross section, and minimum at the corners. If the excitation is at 400 Hz, which is below the cutoff frequency of any non-planar mode, then the contribution of all non-planar modes will decay as the pressure wave travels down the tube. The z variation of the first four modes at 400 Hz is shown in Figure 7. Only the planar mode travels to the end of the tube without decay. Below $f_{cutoff}(l,m)$, the amplitude of non-planar wave mode (l,m) decays with z. The distance at which the amplitude of the pressure contribution from mode (l,m) decays down to 5% of its original pressure can be estimated by

$$x_{5\%}(l,m) = \frac{3c}{2\pi f_{cutoff}(l,m)} \tag{29}$$

The above calculation and Figure 7 show that the waves in the tube should be essentially planar around .75m or more from the speaker.

The distribution of the acoustic pressure amplitude over the cross section is the sum of the contributions of all modes. Since most of the modes decay as the wave travels down the tube, the shape of the wavefront changes from the original "paraboloid-like" shape at the speaker to a practically planar shape at z = 0.75 m, as shown in Figure 8. Beyond that distance, the wavefront is planar throughout the tube until the waves encounter an object that causes scattering.

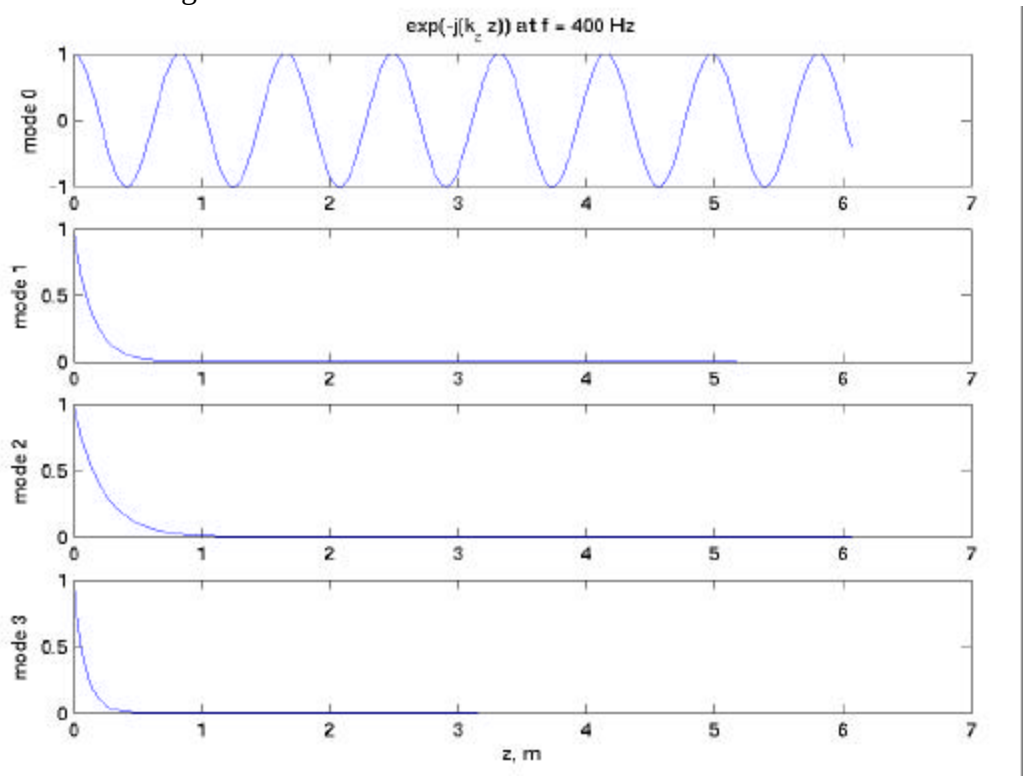

Figure 7. Pressure amplitudes of the first four modes as functions of distance from excitation speaker.

If the excitation frequency is high enough to propagate non-planar modes, then the wavefronts will not be planar even after they travel a long way down the tube. For example, at 1200 Hz, the pressure distribution over the cross section will have the shapes shown in Figure 9 at the distances mentioned in the previous example. Thus, excitation at frequencies higher than the cutoff frequency of the first non-planar mode will result in non-planar waves throughout the tube. Additionally, the shape of the wavefront will vary as the waves travel down the tube.

The above discussion suggests that the tube should be excited at frequencies lower than the cutoff frequency of the first non-planar mode. The resulting planar waves are easy to model. Measurement of the acoustic pressures down the tube can be done at any point in the cross section since the acoustic pressure does not vary with *x* or *y*.

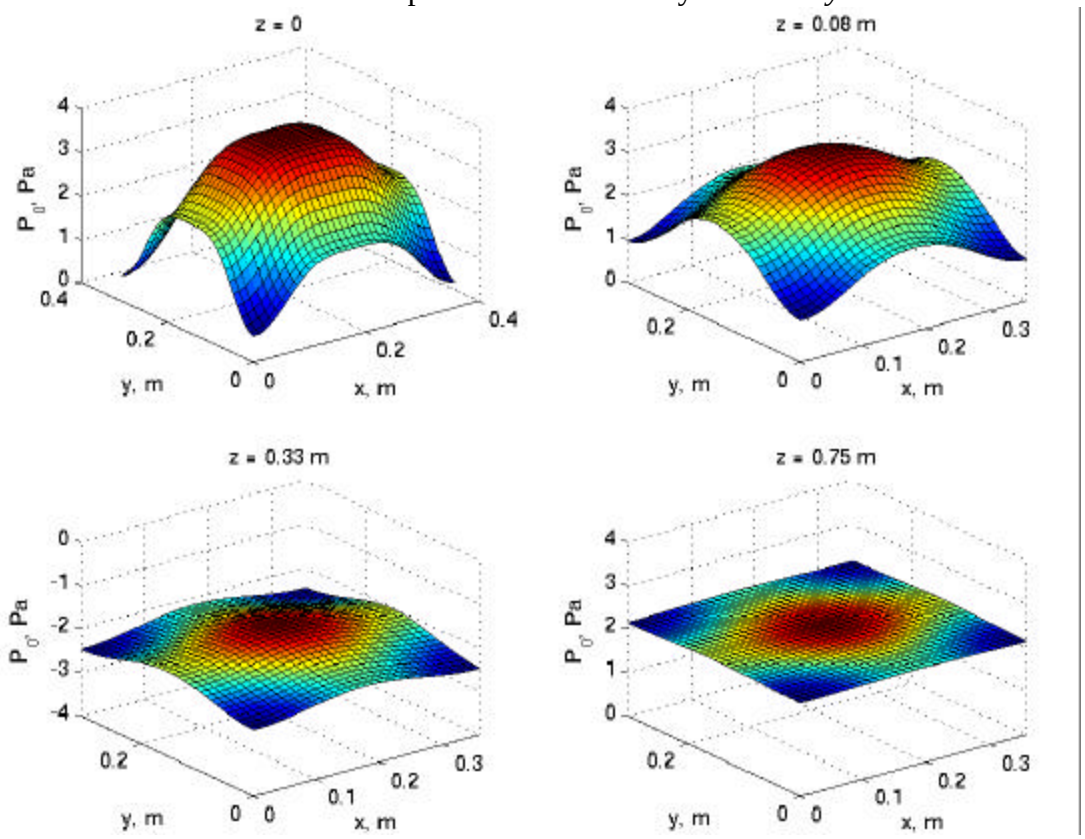

Figure 8. Planarization of pressure waves as they travel down the tube. Excitation frequency = 400 Hz.

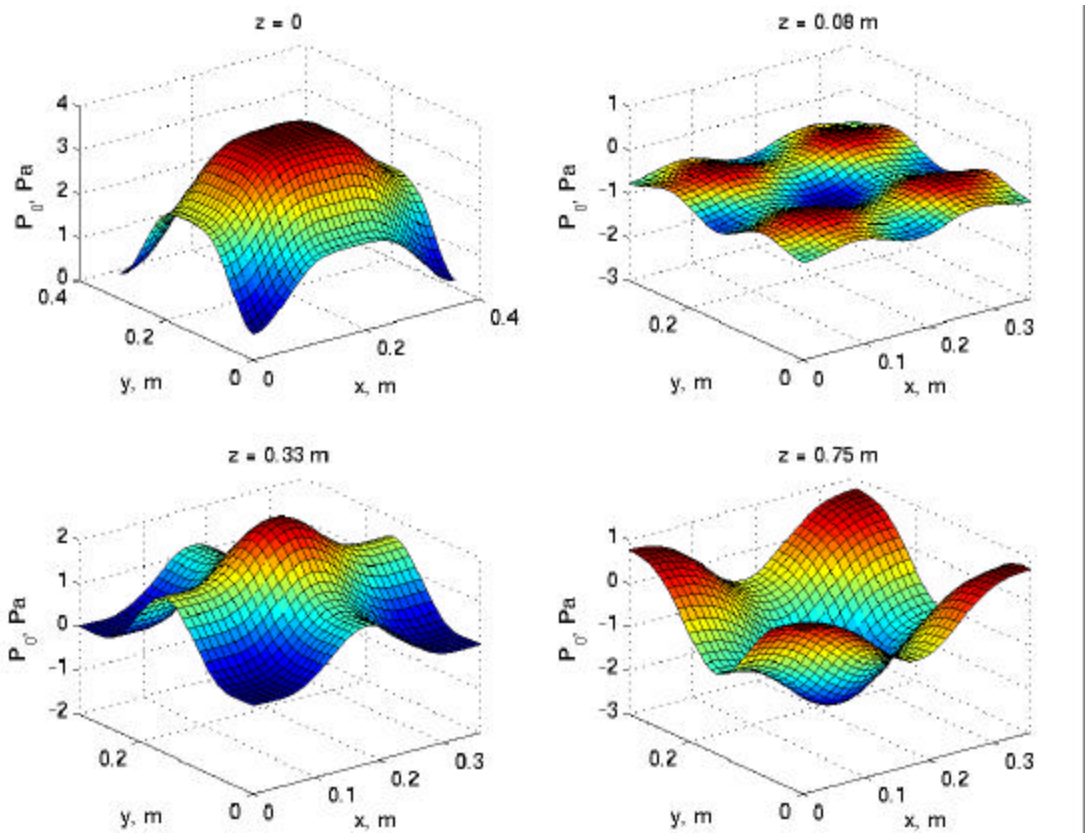

Figure 9. Lack of planarization of pressure waves as they travel down the tube. Excitation frequency = 1200 Hz.

To verify that only planar modes reach the microphones, the following procedure can be used.

- Measure acoustic pressures over a cross section at z = 1 m, with microphones at five points in this cross section -- one at the center of the cross section, and the others close to the four corners of the cross section.
- Excite the tube with a 0-1250 Hz chirp or random sound.
- Plot the phases of sound pressure FRF=$P_{mic}/V_{speaker}$ as functions of frequency for all five microphones.

This procedure resulted in Figure 10, which shows that the five points are in phase for frequencies below 467 Hz. This means that the wave-fronts do not reverse phases below 467 Hz. At higher frequencies, non-planar modes cause the pressure at some quadrants to be out of phase with the pressures at other quadrants or the pressure at the center. The magnitudes of the waves in the four quadrants are shown in Fig. 11, which also shows inter-quadrant variations above 467 Hz. This means that at f > 467 Hz the wave fronts are no longer planar.

Planar waves at the microphones can be used as the excitation boundary condition for the simulation model. For example, this excitation can be represented with a massless rigid piston moving at the appropriate velocity. Around the test object, reflections and scattering by the test object create a three-dimensional, non-planar acoustic field. The non-planar parts of the field die out at a distance from the test object. The microphone

must be placed at a sufficient distance from the test object so that the waves at the microphone are planar. Part of the validation criteria is the agreement between the field measured around the test object and the field resulting from the simulation.

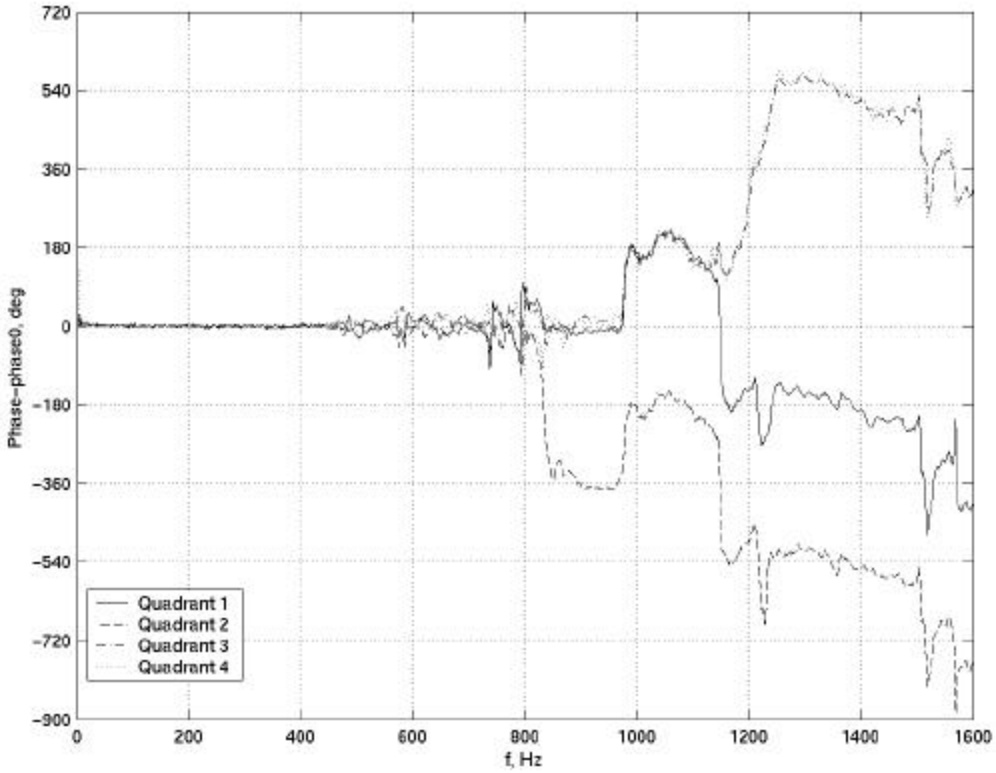

Figure 10. Phases of sound pressure FRFs in four quadrants minus phase of sound pressure FRF at center of cross section.

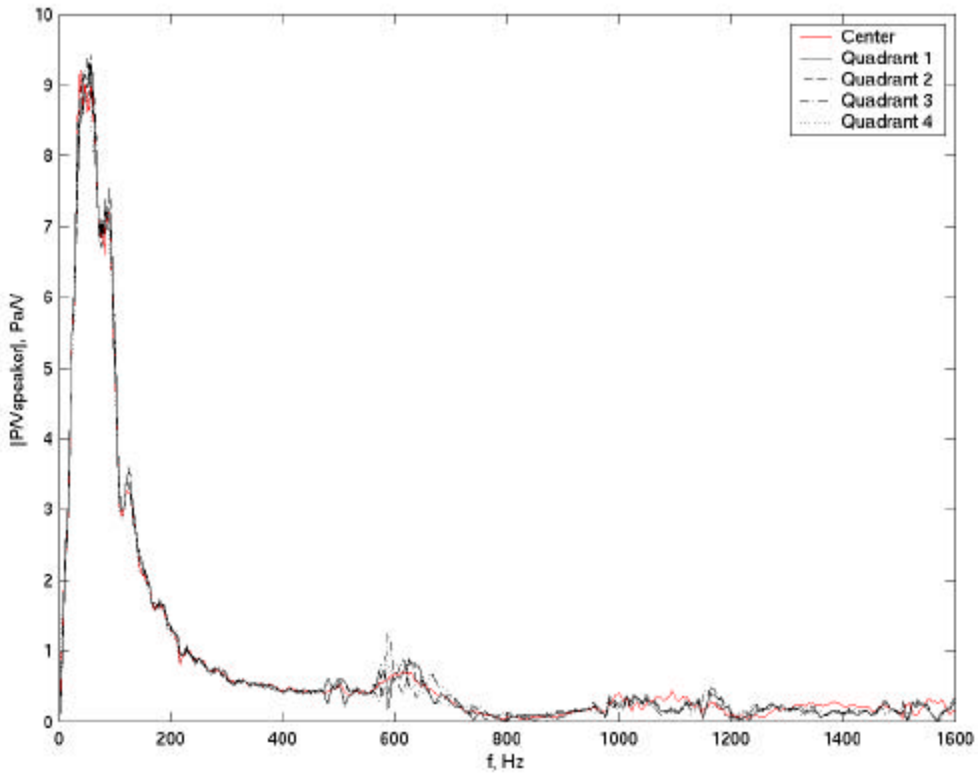

Figure 11. Magnitudes of sound pressure FRFs in four quadrants compared with magnitude of sound pressure FRF at center of cross section.

Modes (0,1) and (1,0) are odd modes, meaning that they are anti-symmetric and have a nodal line in the middle of the cross section of the tube. These anti-symmetric modes are not strongly excited since the excitation speaker is mounted exactly at the center of the cross section of the tube. Phase reversal between quadrants is not strongly observed until the frequency reaches $f_{cutoff}(0,2)$, which is 933 Hz.

Reflection from end

To facilitate modeling, the tube was designed to create traveling waves with minimum reflection from the termination. If the acoustic waves in the tube are planar, the acoustic pressure at any position along the z axis (along the length of the tube) can be expressed as (Kinsler *et al.* 1982)

$$p(z,t) = \left(P_i e^{-jkz} + P_r e^{jkz}\right) e^{jwt} \tag{30}$$

where the wavenumber $k = w/c$. For the purpose of characterizing the tube, the *effective reflection* coefficient is defined as

$$R(f) = P_r(f) / P_i(f) \tag{31}$$

R is a measure of how much of the forward-traveling wave is reflected by the termination. If the tube is clear of any object between the speaker and the termination,

ideally, $P_r = 0$. In practice, this condition of perfectly absorbing termination is difficult to achieve.

If the end of the tube were left open, that end would approximate a zero-pressure boundary condition (at $z = L_z$, $p(t) = 0$ for all t). This boundary condition creates a reflected wave with a pressure that is the negative of the pressure of the incident wave, since the sum of the two waves must be zero at $z = L_z$. A termination at the end of the tube must be designed not to reflect acoustic waves. The absorbing termination pyramid must have a length approximately a half-wavelength at the typical operating frequency. At a sound speed of 332 m/s, a few hundred Hz corresponds to a pyramid length on the order of two meters. In front of the pyramid, the tube should be filled with fluffy materials such as glass wool, with decreasing density towards the test object.

The termination must be tested for its ability to suppress reflection. Any of the following procedures can be used. First, one can launch a short pulse of sound pressure from the excitation speaker, and then record the incident and the reflected waves with a microphone near the speaker. The difference in the peak magnitude of the first pulse and the peak magnitude of the second (reflected) pulse indicates the strength of the reflection at the termination. The reflected wave pressure should be at least 30 dB lower than the incoming wave pressure.

The second procedure is to obtain frequency response functions (FRFs) from the speaker voltage to acoustic pressures at 32 points along the tube. FRF=$P_{mic}/V_{speaker}$. If the wedge is not a perfect absorber, modal analysis of the acoustic field in the tube will show some modes, either real or complex.

Third, one can perform a discrete-Fourier-transformation of the above measured FRF(w,z) = $P_{mic}(w,z)/V_{speaker}(w)$ into the wavenumber domain FRF(w,k) = $P_{mic}(w,k)/V_{speaker}(w)$, and plot the magnitude of the pressures as a function of frequency and wavenumber. Any backward-traveling waves will show some magnitude in the negative wavenumber region of the graph of P as a function of f and k. A typical result of this procedure is shown in Figure 12. Higher reflection coefficients result in more pronounced dispersion curves in the negative wavenumber region. The lower right graph shows a typical case, where the end termination is more effective in absorbing sound at high frequency than at low frequency.

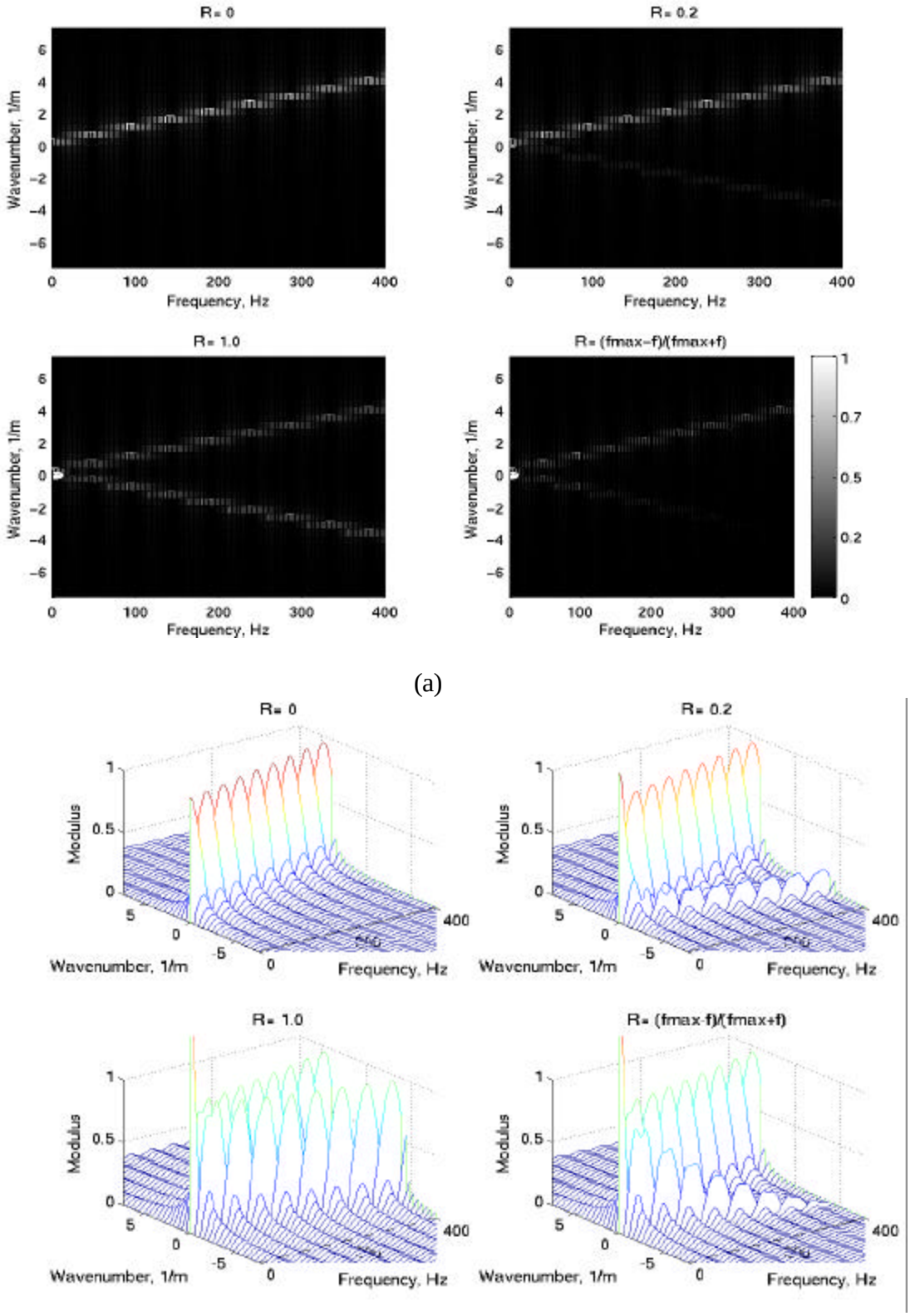

(a)

(b)

Figure 12. Wavenumber transform magnitudes of acoustic pressures along the tube: (a)Two-dimensional view; (b)Three-dimensional view.

A fourth procedure is to separate the sound pressure FRFs from the two microphones into forward-traveling and backward-traveling waves using the procedure described in equations 19 and 20. The termination is a good absorber only if it eliminates almost all of the reflections from the end.

For the tube tested in the laboratory, the FRF from speaker voltage to sound pressure at Mic 2 and Mic 3 were measured and shown in Figure 13. The above separation procedure gave the forward and reflected complex amplitudes, the magnitudes of which are shown in Figure 14. The magnitude of this function is a measure of how much the termination reflects the forward-traveling waves as a function of frequency. The reflection coefficient computed from experimental forward and reflected amplitudes is shown in Figure 15. The "rigid" termination is a board made of the same material and thickness as the tube, attached to the end of the tube. The "open" end is the unflanged end of the tube without added termination. The "ad hoc" termination is a block of acoustic fibers, 0.61m long, stuffed at the end of the tube.

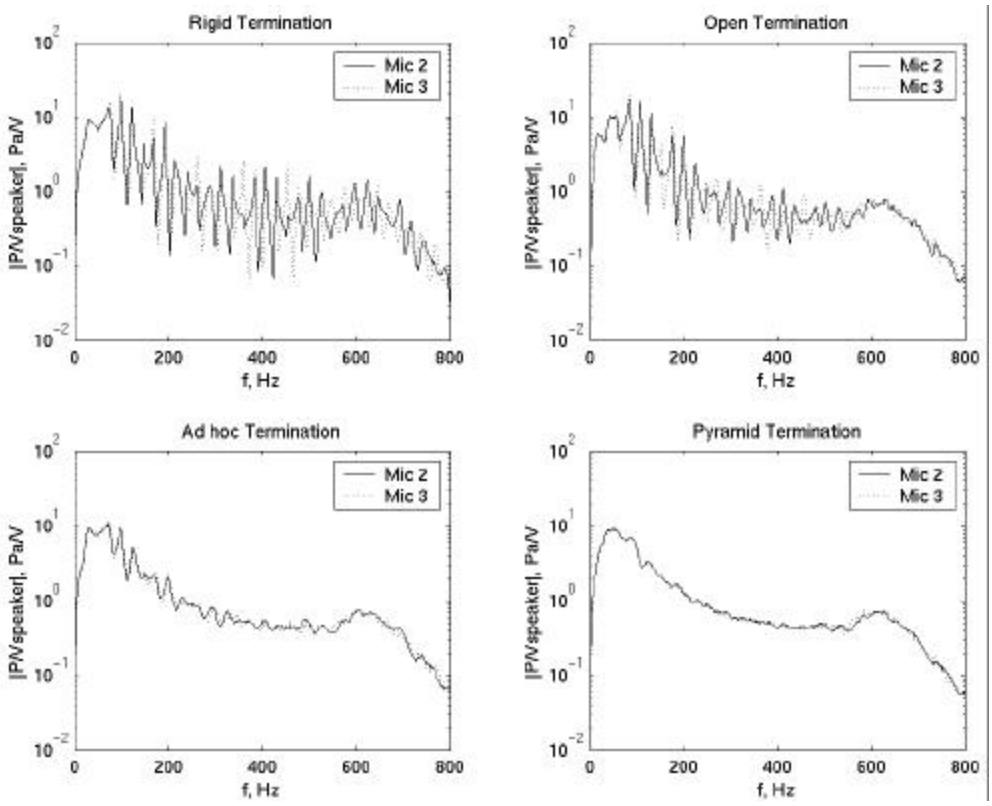

Figure 13. FRF from speaker voltage to sound pressure at Mic 2 and Mic 3.

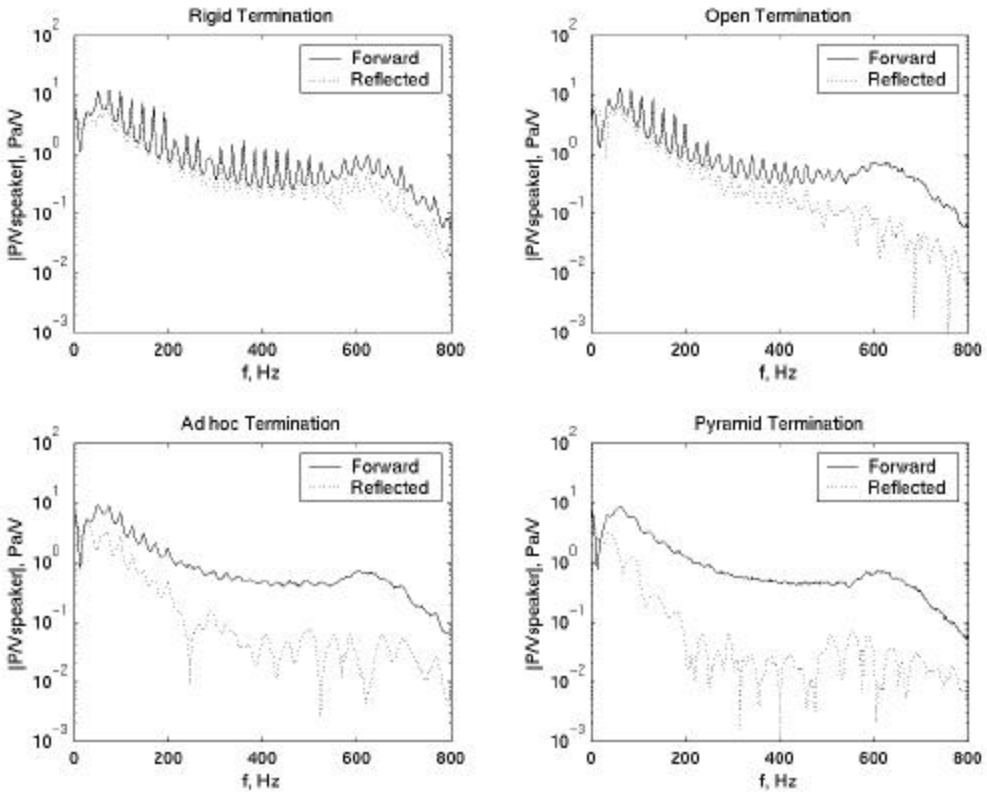

Figure 14. FRFs from speaker voltage to forward and reflected wave amplitudes.

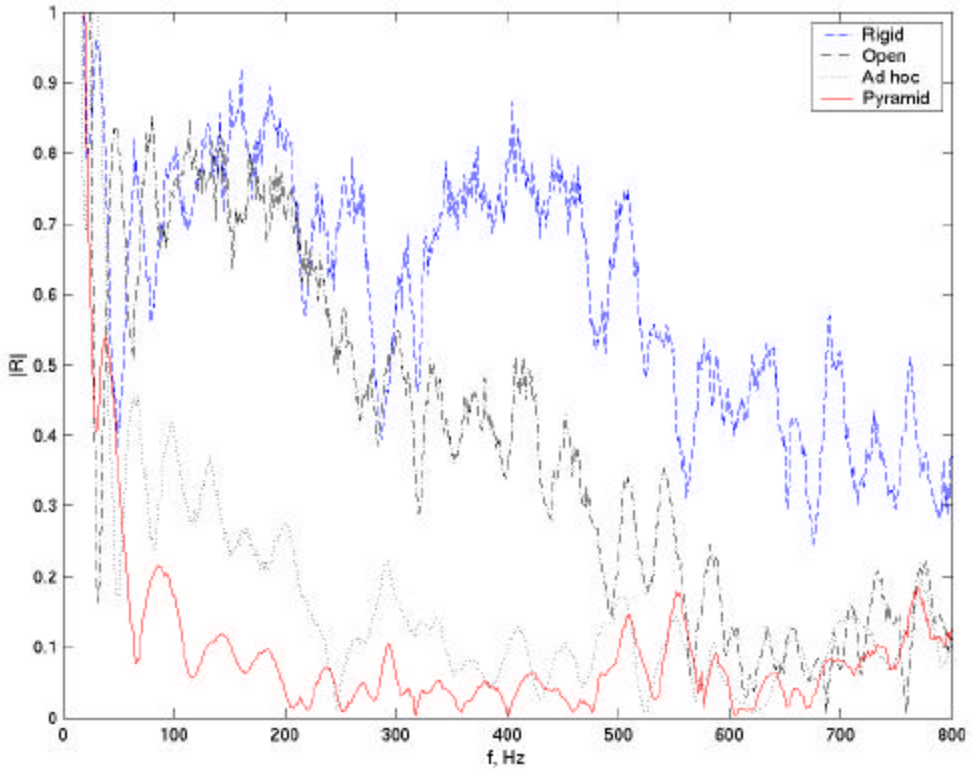

Figure 15. Magnitude of effective reflection coefficient. Various terminations.

Using the wave tube

To fit into the traveling wave tube, the test object may have to be a scaled miniature of the structure to be investigated. The thickness of the miniature must be small enough so that appropriate resonances are excited by the limited bandwidth of the exciting waves. Microphones inside the test objects must be small enough not to disturb acoustic fields inside the test object. If larger microphones are used, they must be properly included in the model.

The positions of Mic 2 and Mic 3 (z_2 and z_3 in Figure 5) must be chosen at a distance where evanescent modes (modes that decay with distance) have died out and the waves are planar. It is also important that the distance between the two microphones, $z_3 - z_2$, does not cause singularity in equations 19 and 20. For a broadband test with a frequency range from 0 to f_{max} to be free from any singularity, the microphones must be placed to satisfy

$$\left|z_3 - z_2\right| < \frac{c}{2 f_{\max}} \tag{32}$$

We would like to obtain frequency response functions (FRFs) from the forward traveling wave to the acceleration at the point on the structure, because this FRF is a property of the structure and should be independent of the excitation. Specifically, for code validation we could like to measure or obtain

$$FRF_{pa}(w) = \frac{a(w)}{P_i(w)} \tag{33}$$

The forward traveling wave complex amplitude, $P_i(w)$, cannot be measured directly. Therefore, FRF_{pa} must be computed from other FRFs that can be easily obtained with an FFT analyzer, such as

$$FRF_{2a}(w) = \frac{a(w)}{p_2(w)} \tag{34}$$

and

$$FRF_{23}(w) = \frac{p_3(w)}{p_2(w)} \tag{35}$$

To obtain the desired FRF_{pa} from the measured FRF_{2a} and FRF_{23}, we use

$$FRF_{pa}(w) = \frac{a(w)}{p_2(w)} F_c(w) \tag{36}$$

That is, we multiply the measured FRF_{2a} with a "correction" function

$$F_c(w) = \frac{p_2(w)}{p_i(w)} = \frac{2j\sin\left(\frac{(z_3 - z_2)}{c}w\right)}{\exp\left(j\frac{z_3}{c}w\right) - \exp\left(j\frac{z_2}{c}w\right)\frac{p_3(w)}{p_2(w)}} \tag{37}$$

This function is in turn derived from the measured $FRF_{23}(w) = \frac{p_3(w)}{p_2(w)}$. Thus, we are able to obtain the FRF from the forward traveling wave to the acceleration at the point on the structure. This FRF can be compared directly with the FRF from the simulation, and serves as a means for validating the code or the model.

4 Experimental Validation of Model

In the following example, the finite element mesh modeled the air in the tube with acoustic elements, and the plate with hexshell elements. Hexshell elements have the topology of solid 3D elements, but with a very similar bending behaviour as shell elements. The excitation was accomplished with a prescribed velocity boundary condition near the acoustic sources. This condition is a Neumann boundary condition for acoustic excitation, and produced plane waves in the tube. First order absorbing boundary conditions were placed at the far end of the tube.

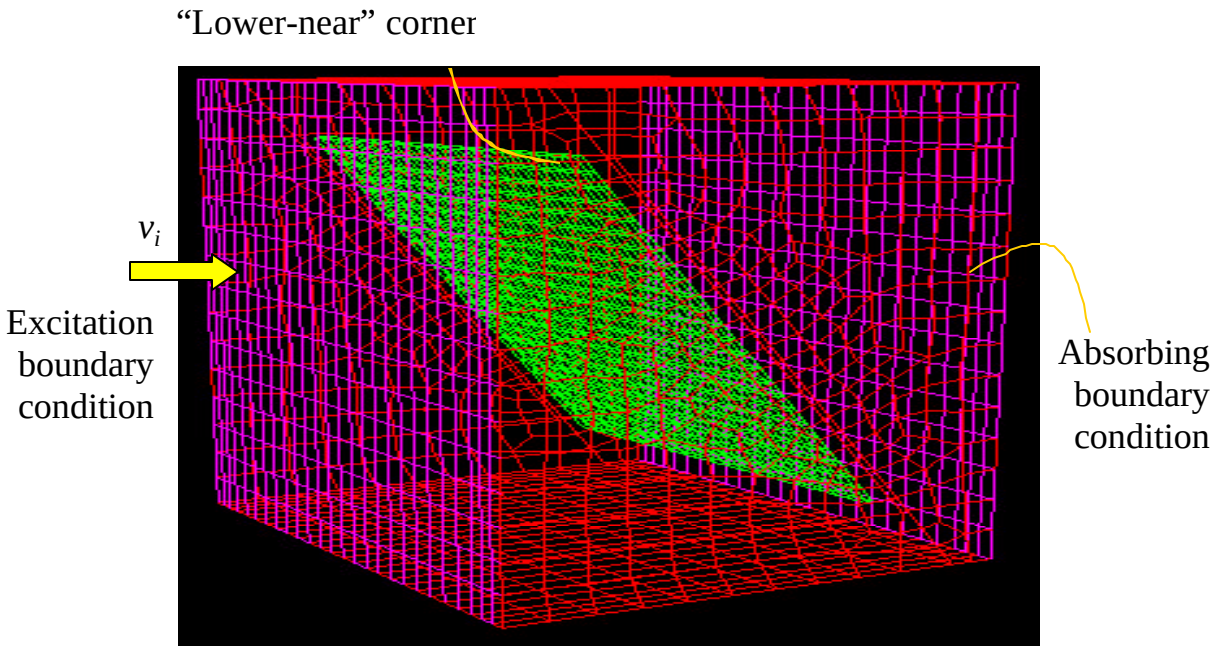

Figure 16. Mesh Used in Validation. Looking from Bottom of Tube.

The planar wave tube was used for validating the finite element calculation. For this purpose, the plate was mounted near the middle of the length of the tube, at an angle of 30^o from the cross section. Accelerometers were placed at the "lower-near" corner (see Figure 5), the center of the plate, and at the "upper far" corner (diagonally opposite the lower near corner). Frequency response functions were recorded. Equation 33 was then used to obtain the frequency response functions from the complex amplitude of the forward-traveling wave to the plate velocity. The result for the center of the plate is shown in Figure 17 and compared with the FRF from the simulation. Two figures are shown in Figure 17. The first (a) shows the direct experiment/simulation comparison, whereas the second (b) shows the results after a scaling by a factor of two (applied to either the experiment or simulation results). It appears that the results differ by a factor of two, though at the time of this writing, the authors do not know whether this additional scaling factor is associated with an error in the simulation results or the experimental measurement.

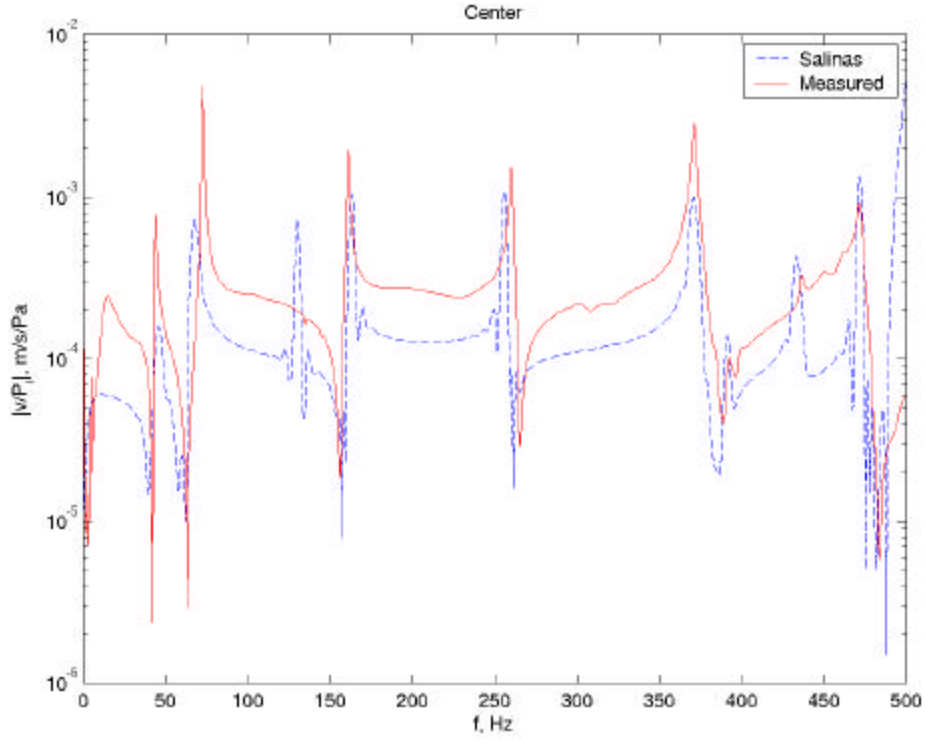

(a) without factor of 2 scaling

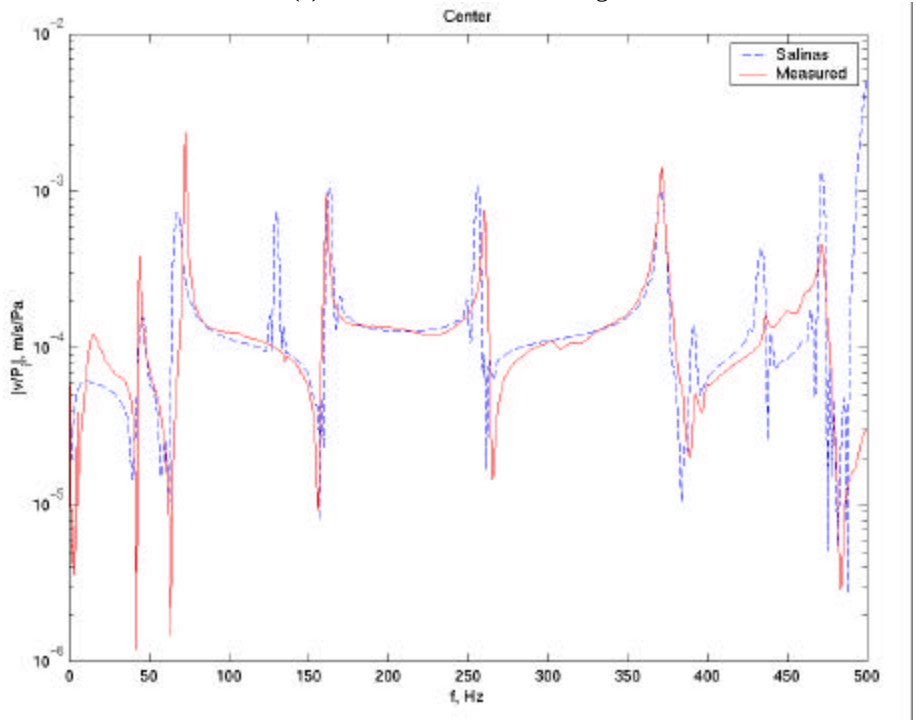

(b) with factor of 2 scaling

Figure 17. Frequency Response Functions from Forward Wave Complex Amplitude to Acceleration at Center of Plate. Dashed Line = FEM, Solid Line = Experiment.

The experiment was repeated at a point near the lower-near corner shown in Fig. 5. The comparison between the FRF from the Salinas simulation and the measured FRF is shown in Figure 18. Lastly, for the upper-far corner, the comparison between the FRF from the simulation and the measured FRF is shown in Figure 19. We note that no factor of 2 scaling was applied in generating the comparisons in Figures 18 and 19.

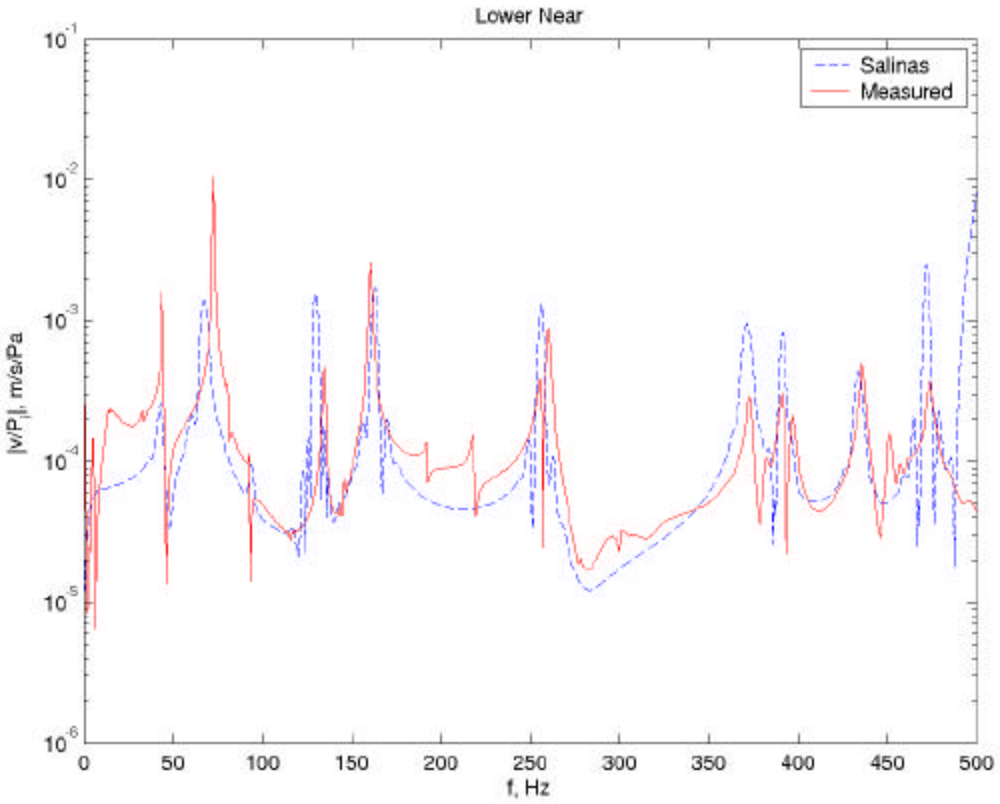

Figure 18. Frequency Response Functions from Forward Wave Complex Amplitude to Acceleration near "Lower Near" Corner. Dashed Line = FEM, Solid Line = Experiment.

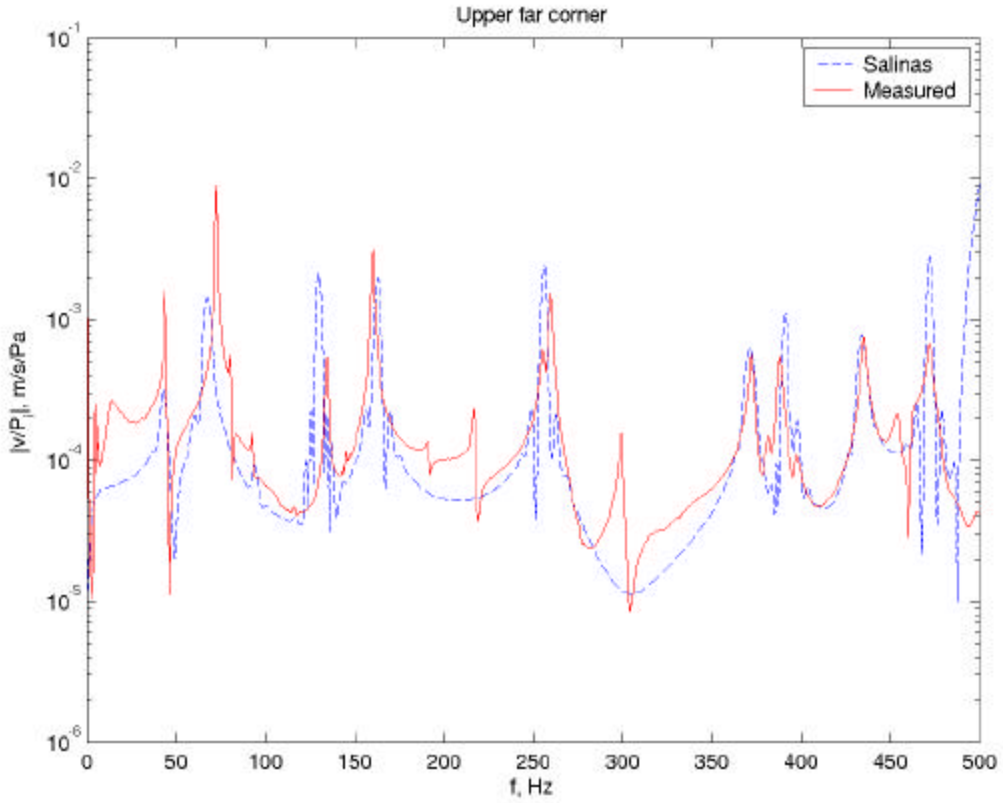

Figure 19. Frequency Response Functions from Forward Wave Complex Amplitude to Acceleration near "Upper Far" Corner. Dashed Line = FEM, Solid Line = Experiment.

4.0 Micro-Torsional Disk Experiment

In many micromechanical devices, a significant amount of energy is lost due to fluid damping. This can hinder the performance of the device by requiring larger amounts of power, reduced sensitivity, or slow structural response. These losses are often classified into two categories -

squeeze-film damping and
damping due to lateral oscillations.

Squeeze-film damping occurs when a fluid is pressed between two surfaces. This pressing produces fluid motion that gives rise to viscous flow and energy loss. This category of energy loss has been well studied using both numerical and closed form analysis.

Damping due to lateral oscillations occurs due to the shearing of fluid and is far less studied. In recent work, [Y. Cho et al., 1993, 1994] showed that a viscous wave approach could be used to describe this type of energy loss. They produced enhanced predictions of damping in a vibrating comb drive by coupling the motion of the drive to a viscous wave solution. In another investigation, [Wenzel, 1982] also used this type of approach to

account for energy losses in a flexural plate wave sensor operating below coincidence. Neglecting edge effects, [Wenzel, 1982] solved for the coupling between the plate and fluid in closed form. Later, [Dohner, 1998] expanded upon Wenzel's analytical work by including edge effects. He was able to show that a fluid/structure resonance occurs near to coincidence. This resonance can draw enough energy from the plate as to render a sensor nonfunctional. Nevertheless, his analysis assumed that existing theory for viscous wave propagation was valid at the micro level.

To further understand the effects of viscous wave propagation on micro devices, test structures were manufactured using SUMMiT V™ technology. Figure 20 illustrates one of these structures. This structure consists of an annular disk of 400um radius at a fixed distance above the substrate. The center of the disk is connected to a torsional spring. Two micro disks were considered - one with a gap of 10.5um above the substrate and the other with a gap of 2.0um above the substrate.

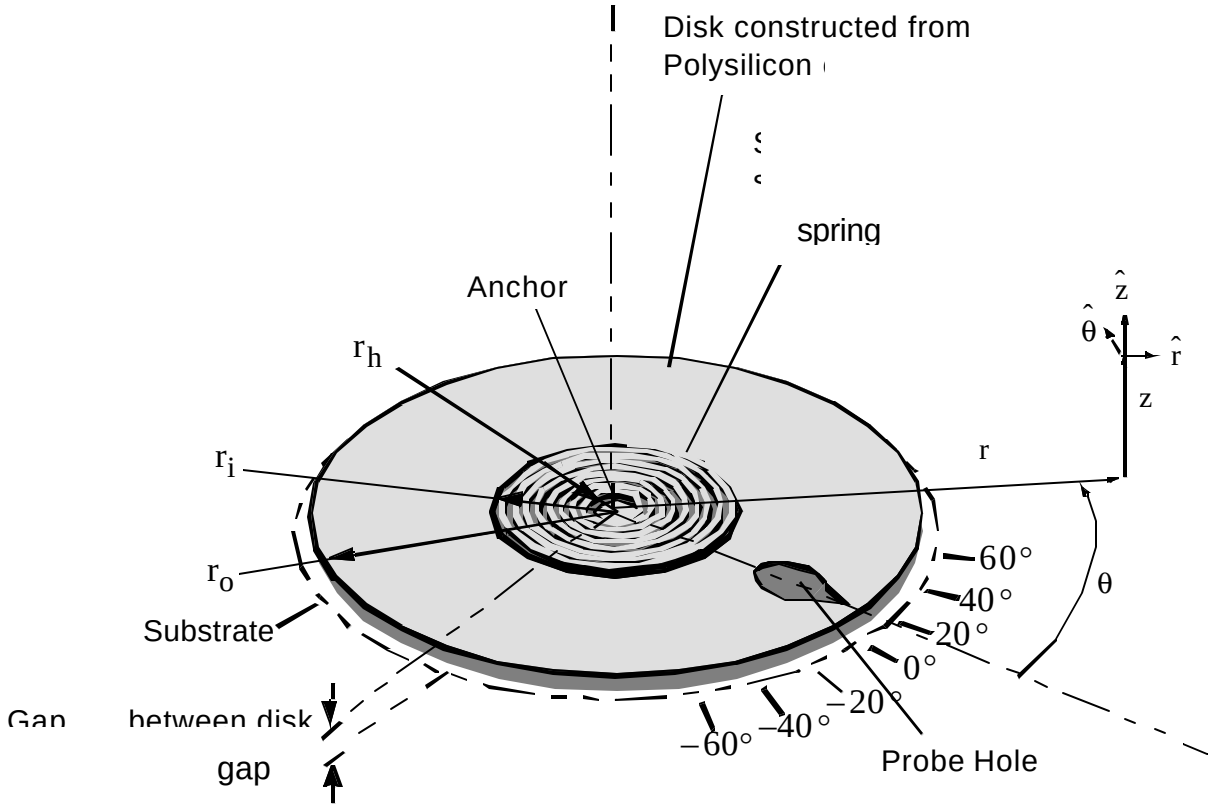

Figure 20. Micro-torsional disk for acoustic shear wave experiment.

The free response of these test structures were obtained by winding the annular disk using a micro probe and recording the response using a high-speed camera connected to a

microscope. The recorded response was then compared to numerical models constructed using relatively mature theory. It was found that theory did not match experiment.

In Figure 21, the free responses of the 10.5um and 2.0um disks are shown. From existing theory, the 2.0um disk should have had an over damped response. Instead, the damping coefficient was about 0.1 –closely resembling the response from the 10.5um disk. The 10.5um response was closer to what was expected.

Existing theory should have predicted both responses quite closely, however, the 2.0um disk results were over an order of magnitude off – surprisingly, in the direction of damping reduction. We consider this a very positive result in that a reduction of damping in a device it is far more difficult to obtain than an increase. The difficulty is now to explain why it occurred.

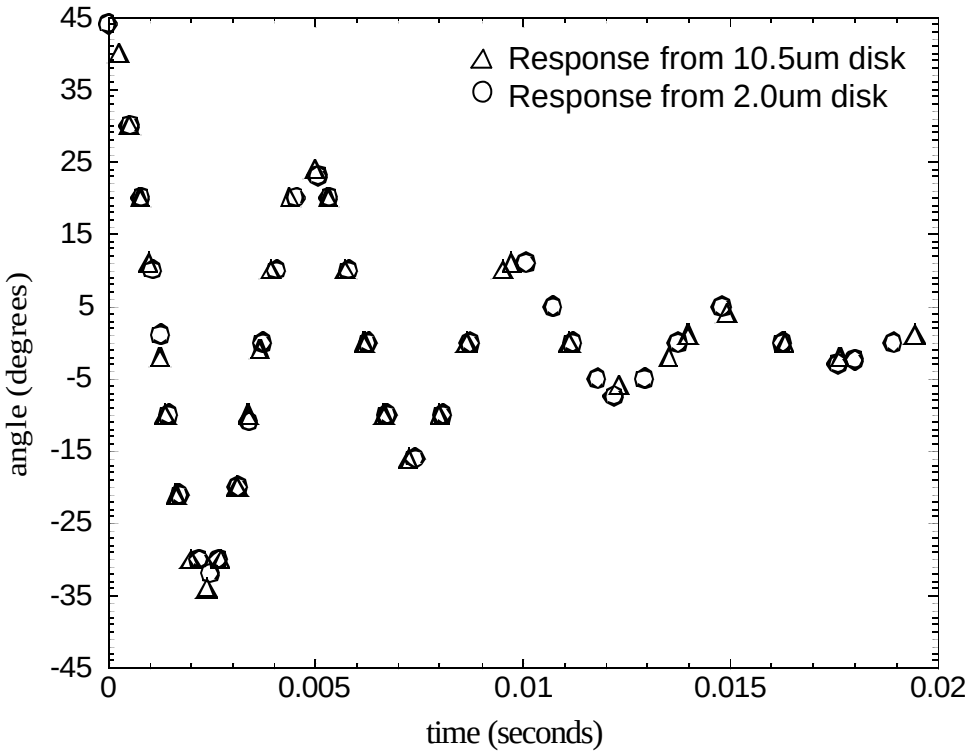

Figure 21. Response of microdisk for two different gap thicknesses.

5.0 Conclusions

In this report, two acoustic formulations for coupled structural acoustics have been described and implemented. For the computational work, a viscous acoustic formulation, and a massively parallel implementation were the main areas of research. Results from

the simulations compared well with experimental results from wave tube experiments. The experimental portion of this work consisted of an acoustic wave tube, and a micro disk for acoustic shear wave experiments. The acoustic wave tube was developed from inexpensive laboratory components and was shown to be an effective means of testing coupled structural acoustic interactions. The wave-guide theory used to derive analytical expressions for the wave tube assumed that the walls were rigid, and that there was no structural-acoustic coupling between the air and the tube walls. This report also provided guidelines for designing and using an acoustic plane wave tube. The limitations of the technique and the validity of the assumptions must be carefully determined by testing the tube before using it. The micro-torsional disk was designed and tested for the purposes of examining acoustic shear wave dissipation in MEMS. The results, which contradicted existing theory, indicated that the damping factors did not depend on the gap thickness. This issue warrants further investigation.

Acknowledgment

The authors are very grateful to Greg Tipton for assistance in constructing the finite element meshes used in the coupled simulations for this report.

This work was conducted at Sandia National Laboratories. Sandia is a multi-program laboratory operated under Sandia Corporation, a Lockheed Martin Company, for the United States Department of Energy under Contract DE-AC04-94-AL85000.

References

D. F. Aldridge, Acoustic Wave Equations for a Linear Viscous Fluid and an Ideal Fluid, *SAND2002-2060*, July 2002.

A. Bermudez and R. Rodriguez, Finite Element Computation of the Vibration Modes of a Fluid-Solid System, *Comput. Methods Appl. Mech. Engrg*., Vol. 119, pp. 355-370, 1994.

M. Bhardwaj, D. Day, C. Farhat, M. Lesoinne, K. Pierson, and D. Rixen. Application of the FETI method to ASCI problems - scalability results on one thousand processors and discussion of highly heterogeneous problems. *Int. J. Numer. Meth. Engrg*., 47:513--535, 2000.

B. Blackstock and M. Hamilton, *Nonlinear Acoustics*, Academic Press, 1998.

H. C. Chen and R. L. Taylor, Vibration Analysis of Fluid-Solid Systems Using a Finite Element Displacement Formulation, *Int. J. Numer. Meth. Engng.*, Vol. 29, pp. 683-698, 1990.

Y.-H. Cho, B.M. Kwak, A.P. Pisano and R.T. Howe 1993 *Proc. IEEE Micro Electro Mechanical Systems Workshop (MEMS'93), Fort Lauderdale, FL, USA, Feb. 7-10,* 93-98. Viscous energy dissipation in laterally oscillating planar microstructures.

Y.-H. Cho, B.M. Kwak, A.P. Pisano and R.T. Howe 1994 *Sensors and Actuators A,* 40, 31-39. Slide film damping in laterally driven microstructures.

J.L. Dohner 1998 *Journal of Sound and Vibration*, **217**(1), 113-126. The contribution of radiation and viscous loss in a fluid loaded flexural plate wave sensor.

G. C. Everstine, Finite Element Formulations of Structural Acoustics Problems, *Computers and Structures,* Vol. 65, No. 3, pp. 307-321, 1997.

C. Farhat, A Lagrange multiplier based on divide and conquer finite element algorithm. *J. Comput. System Engrg*, 2:149--156, 1991.

C. Farhat, M. Lesoinne, and K. Pierson, A Scalable Dual-Primal Domain Decomposition Method, *Numer. Lin. Alg. Appl.*, Vol. 7, pp. 687-714, 2000.

C. Farhat, B. Maman and G. Brown, Mesh partitioning for implicit computations via iterative domain decomposition: impact and optimization of the subdomain aspect ratio, IJNME, 38, 989-1000, 1995.

C. Farhat, M. Lesoinne, P. Le Tallec, K. Pierson, and D.Rixen. FETI-DP: A dual-primal unified FETI method -- part I: A faster alternative to the two-level FETI method. *Int. J. Numer. Meth. Engrg*., 50:1523--1544, 2001.

C. A. Felippa and R. Ohayon, Mixed Variational Formulation of Finite Element Analysis of Acousticelastic/Slosh Fluid-Structure Interaction, *J. Fluids Structures*, Vol. 4, pp. 37-55, 1990.

M. A. Hamdi, Y. Ousset, and G. Verchery, A Displacement Method for the Analysis of Coupled Fluid-Structure Systems, *Int. J. Numer. Meth. Engng.*,Vol. 13, 139-150, 1978.

L. E. Kinsler, A. R. Frey. A. B. Coppens. and J. V. Sanders 1982 *Fundamentals of Acoustics*. 3rd ed. New York: Wiley. p 216-221.

K. Klody. The original concept for the microtorsional structure was developed by Kelly Klody, Electromechanical Engineering, Sandia National Laboratories.

J. Mandel, An Iterative Substructuring Method for Coupled Fluid-Solid Acoustic Problems, *J. Comp. Phys.*, Vol. 177, pp. 95-116, 2002.

H. Morand and R. Ohayon, Substructure Variational Analysis of the Vibrations of Coupled Fluid-Structure Systems. Finite Element Results., *Int. J. Numer. Meth. Engng.* Vol. 14, pp. 741-755, 1979.

E.R. Shepherd *Sandia Report SAND2002-2773C, Sandia National Laboratories, Albuquerque, NM.* Prototyping with SUMMiT technology, Sandia's Ultra-planar multi-level MEMS technology.

S. Temkin, Elements of Acoustics, John Wiley & Sons, 1981.

S.W. Wenzel 1982 *Ph.D Thesis, Department of Electrical engineering and Computer Sciences, University of California, Berkeley, CA.* Applications of ultrasonic lamb waves.

E. L. Wilson and M. Khalvati, Finite Elements for the Dynamic Analysis of Fluid Solid Systems, *Int. J. Numer. Meth. Engng.,* Vol. 19, pp. 1657-1668, 1983.

Distribution:

1	MS0553	David O. Smallwood, 9124
1	MS0557	Thomas J. Baca, 9125
1	MS0557	Jerome S. Cap, 9127
1	MS0557	Thomas G. Carne, 9124
1	MS0557	Paul A Larkin, 9127
1	MS0557	Todd W. Simmermacher, 9124
1	MS0557	Hartono Sumali, 9124
1	MS0557	Gregory D. Tipton, 9125
1	MS0750	David Aldridge, 6116
1	MS0819	Mark A. Christon, 9231
1	MS0824	Wahid L. Hermina, 9110
1	MS0824	Jaime L. Moya, 9130
1	MS0825	Basil Hassan, 9115
1	MS0826	James R. Stewart, 9143
1	MS0826	Steven N. Kempka, 9113
1	MS0834	Michael R. Prairie, 9112
1	MS0835	Kenneth F. Alvin, 9142
1	MS0835	Edward A. Boucheron, 9141
1	MS0835	Jason D. Hales, 9142
1	MS0835	J. Michael McGlaun, 9140
1	MS0835	Kendall H. Pierson, 9142
1	MS0835	Timothy F. Walsh, 9142
1	MS0847	Manoj K. Bhardwaj, 9142
1	MS0847	Clark R. Dohrmann, 9124
1	MS0847	Clay W.G. Fulcher, 9127
1	MS0847	Arne S. Gullerud, 9142
1	MS0847	Joseph Jung, 9127
1	MS0847	Samuel S. Key, 9142
1	MS0847	Harold S. Morgan, 9120
1	MS0847	James M. Redmond, 9124
1	MS0847	Garth M. Reese, 9142
1	MS0847	Howard P. Walther, 9127
1	MS0980	Bob Mata, 5711
1	MS1033	Douglas S. Drumheller, 6211
1	MS1080	David R. Sandison, 1769
1	MS1110	David M. Day, 9214
1	MS1110	Ulrich L. Hetmaniuk, 9214
1	MS1110	David E. Womble, 9214
1	MS1165	Lawrence E. Larsen, 15300
1	MS1310	Jeffrey L. Dohner, 1769
1	MS9018	Central Technical File, 8945-1
2	MS0899	Technical Library, 9616
1	MS0323	LDRD office, 1011